MASTERARBEIT | MASTER'S THESIS

Titel | Title

Interferometric Autocorrelation via 2-Photon Absorption in the near-IR spectral region

verfasst von | submitted by

Felix Harfmann BSc

angestrebter akademischer Grad | in partial fulfilment of the requirements for the degree of

Master of Science (MSc)

Wien | Vienna, 2025

Studienkennzahl lt. Studienblatt | Degree programme code as it appears on the student record sheet:	UA 066 876
Studienrichtung lt. Studienblatt | Degree programme as it appears on the student record sheet:	Masterstudium Physics
Betreut von | Supervisor:	Assoz. Prof. Dipl.-Phys. Dr. Oliver H. Heckl

Abstract

This thesis describes the theoretical background and practical implementation of an interferometric autocorrelation setup for the retrieval of pulse widths of mode-locked laser systems such as optical frequency combs. The system relies on 2-photon absorption (2PA) in semiconductors as the nonlinear process required for pulse width characterization. In 2PA, the energy bandgap of the semiconductor is bridged state by 2 quasi-simultaneously arriving photons via an intermediate virtual quantum state. This enables the possibility of pulse characterization across different wavelength regimes by simply choosing a detector whose bandgap energy allows for 2PA. While readily available silicon detectors are well suited for 2PA in the established wavelength for fiber-optic telecommunication, approximately 1.5 µm, Indium Gallium Arsenide (InGaAs) detectors can extend the application of this method into the mid-infrared, a spectral region of research interest due to a wide range of molecules having their characteristic absorption lines in this regime.

The setup of a collinear Michelson-Interferometer, as well as the design and construction of a detector mechanism using commercially available p-n photodiodes and finally amplification using commercially available microelectronics is outlined. The maximum pulse duration that can be measured depends on the maximum displacement of the delay stage, which in this case comprises a loudspeaker powered by a signal generator, allowing for characterization of pulses up to ≈ 1.3 ps.

Two different ways to measure the pulse width are presented; the interferometric autocorrelation approach, which relies on counting of interference fringes, as well as the intensity autocorrelation approach, requiring additional characterization and calibration of the interferometers delay stage. Pulse quality is characterized using a simple approach which compares the experimentally computed value for the time-bandwidth product with its transform-limited counterpart.

Pulse durations were retrieved for an Erbium Dual-Comb laser system emitting at a center wavelength of $\lambda = 1570$ nm with spectral widths varying between $\Delta\lambda = 17.26$ nm and $\Delta\lambda = 20.1$ nm using a commercially available silicon photodiode, yielding FWHM pulse widths of about 240 fs. Additionally, we aimed to characterize the change in pulse duration as pump currents of the individual amplification stages were increased, but unfortunately an undesired onset of multi-pulsing was observed.

Pulse duration measurements were also attempted for a laser system based on an amplified Ytterbium-doped nonlinear amplifying loop mirror with non-reciprocal phase bias using a homebuilt detector, including a homebuilt transimpedance amplifier. Unfortunately the nonlinear signal induced in the photodiode was too weak to make accurate statements about pulse duration of this laser system.

Abstract

Diese Arbeit beschreibt die theoretische Basis sowie praktische Umsetzung eines interferometrischen Autokorrelators zur Messung der Pulsbreiten von moden-gekoppelten Lasersystemen, wie beispielsweise optischen Frequenzkämmen. Das System basiert auf der Zwei-Photonen-Absorption (2PA) in Halbleitern als nichtlinearem Prozess, der zur Charakterisierung der Pulsdauer benötigt wird. Bei 2PA wird die Bandlückenenergie des Halbleiters durch zwei nahezu gleichzeitig eintreffende Photonen über einen virtuellen Quantenzustand überbrückt.
Auf diese Weise kann die Pulsmessung über weite Wellenlängenbereiche hinweg durchgeführt werden, indem ein Detektor gewählt wird, welcher im gewünschten Wellenlängenbereich 2PA sensitiv ist. Während Siliziumdetektoren für 2PA im Telekommunikationswellenlängenbereich von etwa 1.5 µm geeignet sind, kann das Konzept mit Hilfe von Indium-Gallium-Arsenid (InGaAs) Detektoren in den mittleren Infrarotbereich erweitert werden, welcher von besonderem Forschungsinteresse ist, da eine Vielzahl an verschiedenen Molekülen ihre charakteristischen Absorptionslinien aufweist.
Der Aufbau eines kollinearen Michelson-Interferometers, das Design und Erstellung des Detektors unter Verwendung handelsüblicher p-n-Photodioden sowie die darauffolgende Verstärkung mittels kommerziell erhältlicher Mikroelektronik wird erläutert. Die maximal messbare Pulsdauer hängt von der Maximalauslenkung der Verzögerungsstufe ab, welche in diesem Fall aus einem simplen Lautsprecher besteht, welcher von einem Signal-Generator angetrieben wird.
Zwei verschiedene Methoden zur Bestimmung der Pulsbreite werden verwendet: Der interferometrische Ansatz, bei dem Interferenzmaxima gezählt werden sowie der Ansatz der üblichen Intensitätsautokorrelation, welcher eine zusätzliche Charakterisierung und Kalibrierung der Verzögerungseinheit erfordert. Die Pulsqualität kann mit Hilfe eines einfachen Verfahrens bewertet werden, bei dem der experimentell ermittelte Wert des Zeit-Bandbreiten-Produktes mit seinem transformation-limitierten Pendant verglichen wird.
Die Pulsdauer wurden für ein Erbium-Dual-Comb-Lasersystem ermittelt, das bei einer zentralen Wellenlänge von $\lambda = 1570$ nm emittiert und dabei spektrale Breiten von $\Delta\lambda = 17.26$ nm bis $\Delta\lambda = 20.1$ nm aufweist. Unter Verwendung einer handelsüblichen Silizium-Photodiode konnten Pulsbreiten von etwa 240 fs bestimmt werden. Darüber hinaus wurde versucht, die Abhängigkeit der Pulsdauer bei Erhöhung der Pumpströme in den einzelnen Verstärkerstufen zu charakterisieren, wobei hierbei unerwünschtes Multipulsing beobachtet werden konnte.
Zudem wurden Messungen der Pulsdauer an einem Lasersystem auf Basis eines verstärkten, Ytterbium-dotierten NALM Lasers versucht. Hierbei kam ein eigens gebauter Detektor inklusive eines selbstentwickelten Transimpedanzverstärkers zum Einsatz. Leider erwies sich das in der Photodiode induzierte nichtlineare Signal als zu schwach, um verlässliche Aussagen über die Pulsdauer dieses Lasersystems treffen zu können.

Contents

1 Introduction **1**

2 Theoretical Background **2**
2.1 Optical Autocorrelation . . . 2
2.1.1 Field Autocorrelation . . . 2
2.1.2 Intensity Autocorrelation . . . 3
2.1.3 Interferometric Autocorrelation . . . 4
2.2 Pulse Characterization . . . 7
2.2.1 Time Bandwidth product . . . 7
2.2.2 Pulse Quality & Chirp . . . 7
2.2.3 Light passing through a fiber . . . 9
2.3 Nonlinear Polarization Optics for Harmonic Generation . . . 10
2.3.1 Second order nonlinear processes . . . 10
2.3.2 Third order nonlinear processes . . . 11
2.4 Semiconductor optics . . . 12
2.4.1 Linear absorption . . . 12
2.4.2 Nonlinear Multi-Photon Absorption . . . 12
2.4.2.1 Lifetime and degeneracy of 2PA state . . . 15
2.4.2.2 Bandgap dependence of 2PA coefficient . . . 16
2.4.3 Induced 2PA Photocurrent . . . 17
2.5 Photodetector . . . 19
2.5.1 Transimpedance Amplifier Design . . . 21

3 Setup & Results **23**
3.1 Autocorrelator Setup . . . 23
3.1.1 Calibration of delay stage and pulse duration retrieval . . . 24
3.1.2 Photodetector & Amplifier . . . 26
3.2 2PA Results . . . 28
3.2.1 Dependence of induced 2PA current on average input power . . . 28
3.2.2 Z-Scan . . . 28
3.3 Interferometric Autocorrelation Results . . . 30

4 Conclusion and Discussion **35**

A Appendix - Noise Analysis Amplifier Circuit **37**

B Appendix 2 - Table of abbreviations **41**

C References **42**

1 Introduction

Modern applications of pulsed laser systems — such as atmospheric research, chemical analysis, astrophysics, and molecular transition characterization — require a stable and reliable source in order to be able to perform accurate measurements [1]. One measure of characterization of such pulsed lasers is their pulse width τ_P, defined as the full-width half-maximum (FWHM) of the intensity autocorrelation. Combining the pulse width and spectral bandwidth offers initial insights into pulse quality and sets an upper limit for peak pulse power.

Optical autocorrelators are widely used to measure pulse durations using a Michelson interferometer setup: Initially, the incoming pulse to be measured is split into two identical copies at half the intensity using a 50:50 beam splitter. A time delay is introduced by adjusting the path length of one arm before the two pulses are recombined via a nonlinear interaction. The generated nonlinear signal depends on the temporal overlap between the two pulses and is recorded to provide insight into the pulses temporal profile. In order to generate the nonlinear signal, usually one uses nonlinear crystals (e.g. KDP, β-BBO), to produce the second harmonic of the fundamental beam. These crystals require large peak powers as well as the fulfilment of the phase-matching criterion to generate the second harmonic, making the alignment of such systems tedious and requiring re-adjustment whenever a new wavelength is to be measured.

Processes other than second-harmonic generation (SHG) can be used to generate the nonlinear signal and the need for a SHG crystal can be omitted entirely by using a photodetector capable of two-photon absorption (2PA), a quantum process first described theoretically in 1936 by Maria Goeppert-Mayer [2] and first experimentally observed in 1961 [3]. 2PA makes use of quantum mechanical virtual states where two separate photons are absorbed simultaneously within the active layer of the photodiode itself. The obtained interferometric autocorrelation trace provides a more comprehensive method for pulse characterization than intensity autocorrelation as it not only grants access to the pulse duration, but also provides information about pulse asymmetries and chirp, arising due to higher-order interference terms of the individual electric fields.

In order for 2PA to occur, it is crucial to choose a semiconductor photodetector such that the single photon energy $h\nu$ of the laser source is smaller than the bandgap energy (such that linear absorption does not take place), but is larger than half the bandgap energy, allowing the electrons in the photodiode to be excited into a virtual state first. Given that a second photon with similar energy arrives within the virtual states lifetime, the electron gets elevated into the excited state, generating a measurable current flow in the micro- to nanoampere range, which is then amplified using an appropriate current-to-voltage amplification mechanism. The interferometric approach offers the option to characterize pulse widths of laser systems emitting average powers in the low mW range [4, 5, 6, 7]. Furthermore, the bandgap energy condition can be adapted to account for general multiphoton absorption processes, which mathematically generate even higher order interference terms, allowing for real-time characterization of potential pulse asymmetries [8, 9].

In this work, a simple, low-cost autocorrelator based on 2PA is assembled and tested: The Michelson-Interferometer configuration comprises a loudspeaker powered by a signal generator acting as a movable delay stage, a strongly-focusing optical element as well as a detector that fulfils the 2PA bandgap condition for the given wavelength range. In particular, the pulse duration of two different laser systems is investigated:

1) Mode-locked Ytterbium doped nonlinear amplifying loop mirror (NALM) with non reciprocal phase bias ("Seed Laser") [10], center wavelength $\lambda_{\text{center}} = 1.040$ µm using a GaAsP-Photodiode including a home-built transimpedance amplifier.

2) Mode-locked Erbium dual comb (Er-DC), center wavelength $\lambda_{\text{center}} = 1.57$ µm [11] using a commercially available switchable-gain Si-Photodetector by Thorlabs.

2 Theoretical Background

The following chapter will provide an overview of the theoretical concepts required for pulse duration measurements. Chapter (2.1) will provide insight into different types of optical autocorrelation techniques and shows why a simple Fourier Transform Spectrometer (FTS) is not enough to retrieve pulse widths. Next, a mathematical description of the typically deployed non-collinear technique of SHG in nonlinear crystals is given in chapter (2.3). Semiconductor optics including the mathematical model of 2PA and its characteristics is discussed in chapter (2.4). Retrieval of the pulse width using the intensity approach as well as the interferometric approach is outlined in chapter (2.2). Finally, the theory and design of a simple, amplified low-noise photodetector is given in chapter (2.5).

2.1 Optical Autocorrelation

In order to accurately quantify such short timeframes, an even shorter event is required to act as a reference. Unfortunately, commercially available photodiodes and detectors have electrical response times of a few nanoseconds - too long to accurately resolve individual pulses. One solution to this problem is given by using the pulse itself as a reference and scanning across it. This involves splitting the laser pulse into two equal parts in a Michelson-Interferometer and subsequently introducing a time delay $\tau = \frac{2\Delta L}{c}$ to one of the pulses by adjusting the length L of one of the interferometer arms before recombining the electric fields. Depending on the instantaneous applied delay τ, the two recombined electric fields interfere either constructively or destructively, yielding alternating maxima and minima.
Linear detection mechanisms will provide information about the spectrum, as is typically done in Fourier Transform Spectroscopy (FTS). Recombination via 2nd order nonlinear processes are used to recover the pulse width via background-free intensity autocorrelation - even higher-order generation processes can provide insight into possible pulse asymmetries. Modern algorithms such as spectral phase interferometry for direct electric-field reconstruction (SPIDER) [12] and frequency-resolved optical gating (FROG) [13] further provide information about the spectral phase [14].

2.1.1 Field Autocorrelation

Field autocorrelation is the basic principle underlying FTS, a technique which is used to recover the spectral information of a laser by means of recording an interferogram and performing a Fourier transform on it. The typical setup is a collinear Michelson-Interferometer, where a phase shift $\Delta\phi$ is introduced between the two electric fields $E(t)$ by adjusting the length of one of the arms of the interferometer, as depicted in figure (1A). The value of the phase-shift $\Delta\phi$ depends on the optical path difference (OPD) $\Delta L = c\tau/2$ between the two arms:

$$\Delta\phi = \frac{2\pi}{\lambda}c\tau = \frac{\pi}{\lambda}\Delta L = \frac{\pi}{\lambda\cos\theta}(l_2 - l_1) \tag{1}$$

where l_1, l_2 are the lengths of the individual arms of the interferometer and θ is the angle between the light propagation direction and the axis along which the path difference is being introduced.

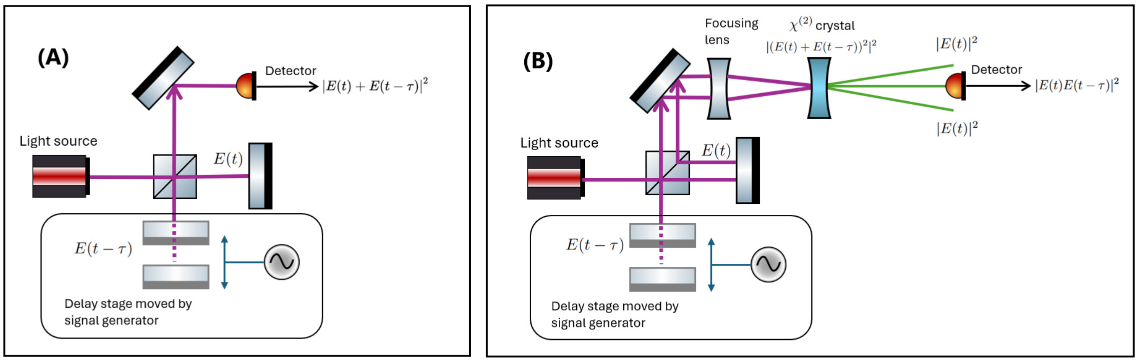

Figure 1: Left: Collinear Michelson Interferometer, typically used in Fourier transform spectroscopy. Right: Typical non-collinear Michelson Interferometer including SHG crystal for background-free intensity autocorrelation. The subtraction of the background is typically conducted by placing an aperture at the output of the $\chi^{(2)}$ crystal such that only the beam propagating along the optical axis is measured by the detector.

Equation (1) determines whether the subsequent interference of the electric fields acts constructively or destructively: A displacement of the mirror by $\lambda/4$, where λ is the wavelength of the used laser will result in an OPD of $\lambda/2$, i.e. the experienced phase shift is equal to π and the two electric fields interfere destructively. The obtained signal includes the field autocorrelation $\Gamma(\tau)_{\text{field}}$ of the original pulse $E(t)$ with the pulse delayed by τ, $E(t-\tau)$.

$$\Gamma(\tau)_{\text{field}} = \int_{-\infty}^{\infty} E(t)E^*(t-\tau)dt \tag{2}$$

The issue that arises here is the fact that photodetectors do not measure the complex electric field $E(t)$ directly, but rather the intensity $I(t) = |E(t)|^2$, limiting the information which can be gathered from such a measurement. By applying the Fourier transform $\mathfrak{F}$ on (2), one only obtains information about the spectral intensity $|\tilde{E}(\omega)|^2$ of the electric field $E(t)$:

$$\mathfrak{F}(\Gamma(\tau)) = \frac{1}{2\pi}\int_{-\infty}^{\infty} |\tilde{E}(\omega)|^2 e^{-i\omega t} d\omega \tag{3}$$

This poses the issue of losing the spectral phase-information $\phi(\omega)$, which would be required to accurately and fully reconstruct the amplitude and phase of the electric field $E(t)$. This is due to the fact that there is an infinite number of time-domain signals that can share the same magnitude spectrum but differ in phase. This is the well-known phase retrieval problem, which states that measuring the autocorrelation of the electric fields is not enough to make statements about the pulse duration [14].

2.1.2 Intensity Autocorrelation

Intensity autocorrelation is commonly used to measure pulse widths through second-harmonic generation in a nonlinear crystal. In background-free **intensity autocorrelation**, a non-collinear Michelson interferometer is used, as depicted in figure (1B). The intensity of the SHG signal depends on the temporal overlap between the two pulses. Because measurable levels of second-harmonic light are generated only when the pulses overlap in time, this process effectively acts as an ultrafast gating mechanism. The nonlinear crystal produces a signal $\propto [E(t) + E(t-\tau)]^2$, however, due to the non-collinear geometry, only the term corresponding to the beam propagating along the optical axis is measured, yielding the intensity autocorrelation $\Gamma_{\mathrm{AC}}(\tau)$:

$$\begin{aligned} \Gamma_{\mathrm{AC}}(\tau) &= \int_{-\infty}^{\infty} I(t) I(t-\tau) dt \\ &= \int_{-\infty}^{\infty} |E(t)E(t-\tau)|^2 dt \end{aligned} \tag{4}$$

having used $I(t) = |E(t)|^2$. Equation (4) is symmetric $\Gamma_{\mathrm{AC}}(\tau) = \Gamma_{\mathrm{AC}}(-\tau)$ and has its maximum at $\tau = 0$. Unfortunately, Equation (4) does not contain a term describing phase, meaning that all information about phase and chirp are lost when performing pulse width measurements using only intensity autocorrelation.

The generation of the second-harmonic light is typically performed inside a nonlinear crystal. The efficiency at producing higher-harmonic light depends on the crystals nonlinear susceptibility $\chi^{(2)}$. Additionally, the phase-matching criterion needs to be fulfilled, meaning that the phases between the two fundamental pulses need to be synchronized temporally inside the crystal such that $\Delta k = 0$. For low femtosecond laser pulses, this poses another issue of having to manage group delay dispersion (GDD) between the two beams as they travel through the crystal [15], such that in order to produce reasonable conversion efficiencies, the crystal thickness needs to be relatively small [16].

2.1.3 Interferometric Autocorrelation

Interferometric autocorrelation (IAC), also sometimes referred to as **fringe-resolved autocorrelation (FRAC)**, makes use of a combination of the previous cases by deploying a collinear geometry, generating second harmonic light, which then interferes with the light of the fundamental beam, as depicted in Figure (9). The method combines several pulse characterization methods that each oscillate at different frequencies (namely at ω and 2ω and a DC term) into a single trace and includes the intensity autocorrelation as one of its terms [14]:

$$\begin{aligned} \Gamma_{\mathrm{IAC}}(\tau) &= \int_{-\infty}^{\infty} |(E(t) + E(t-\tau))^2|^2 \; dt \\ &= \int_{-\infty}^{\infty} |E^2(t) + 2E(t)E(t-\tau) + E^2(t-\tau)|^2 \; dt \end{aligned} \tag{5}$$

multiplying out all terms, one gets the full expression

$$\begin{aligned} \Gamma_{\mathrm{IAC}}(\tau) = \int_{-\infty}^{\infty} & E^2(t)E^{*2}(t) + E^2(t-\tau)E^{*2}(t-\tau) \\ & + 2E^2(t)E^*(t)E^*(t-\tau) + 2E(t)E(t-\tau)E^{*2}(t) \\ & + 2E(t)E(t-\tau)E^{*2}(t-\tau) + 2E^*(t)E^*(t-\tau)E^2(t-\tau) \\ & + E^2(t)E^{*2}(t-\tau) + E^2(t-\tau)E^{*2}(t) \\ & + 4E(t)E(t-\tau)E^*(t)E^*(t-\tau)dt \end{aligned} \tag{6}$$

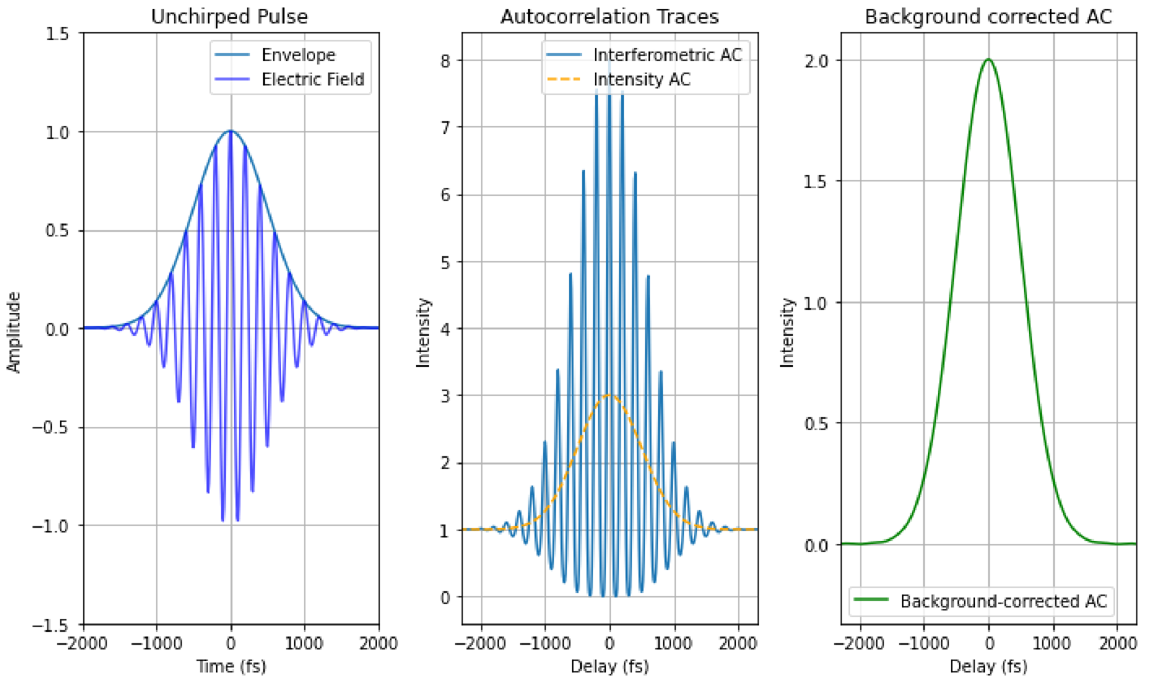

Figure 2: Concept of interferometric autocorrelation. Left: Gaussian pulse in the time domain. Middle: IAC trace of the gaussian pulse with the 8:1 ratio visible (blue). By filtering out the fast oscillating components, one obtains the usual intensity autocorrelation (orange) with a 3:1 ratio from which a pulse duration can be deduced. Right: By further subtracting the DC background term, the 2:0 peak-to-background term is obtained, as would be measured when using a non-collinear beam geometry.

which can be summarized to express the 4 characteristic terms of the fringe resolved autocorrelation, namely a **constant DC background intensity $I_{\mathbf{BG}}$**:

$$\begin{aligned} I_{\mathrm{BG}} &= \int_{-\infty}^{\infty} E^2(t)E^{*2}(t) + E^2(t-\tau)E^{*2}(t-\tau)dt \\ &= \int_{-\infty}^{\infty} I^2(t) + I^2(t-\tau)dt \end{aligned} \tag{7}$$

the **intensity autocorrelation trace, $I_{\mathbf{AC}}$**,

$$\begin{aligned} I_{\mathrm{AC}} &= 4\int_{-\infty}^{\infty} E(t)E(t-\tau)\cdot E^*(t)E^*(t-\tau)dt \\ &= 4\int_{-\infty}^{\infty} I(t)I(t-\tau)dt \end{aligned} \tag{8}$$

The **modified spectrum of $E(t)$, I_ω**,

$$I_\omega = 2\int_{-\infty}^{\infty} [I(t) + I(t-\tau)][(E(t)E^*(t-\tau) + E^*(t)E(t-\tau)]dt \tag{9}$$

and the **interferogram arising from the second harmonic**, $I_{2\omega}$, corresponding to the spectrum of the second harmonic,

$$I_{2\omega} = \int_{-\infty}^{\infty} E^2(t)E^{*2}(t-\tau) + E^{*2}(t)E^2(t-\tau)dt \tag{10}$$

such that the whole trace can be written as

$$\Gamma_{\text{IAC}}(\tau) = I_{\text{BG}} + I_{\text{AC}} + I_\omega + I_{2\omega} \tag{11}$$

For temporarily non-overlapping beams ($\tau \to \infty$), the terms I_{AC}, I_ω and $I_{2\omega}$ are equal to 0 causing the interferometric autocorrelation trace to only consist of the constant background term:

$$\Gamma_{\text{IAC}}(\tau \to \pm\infty) = 2\int_{-\infty}^{\infty} I(t)^2 dt = I_{\text{BG}} \tag{12}$$

As the delay between the two pulses decreases, the two beams start to overlap and interfere. When approaching a delay $\tau \to 0$, the interference fringes of the non-background terms start to become more present, until at the perfect overlap, $\tau = 0$, one finds:

$$\begin{aligned}\Gamma_{\text{IAC}}(\tau \to 0) = & \underbrace{2\int_{-\infty}^{\infty} I^2(t)dt}_{DC\ Background} + \underbrace{4\int_{-\infty}^{\infty} I^2(t)dt}_{Intensity\ Autocorrelation} \\ & + \underbrace{8\int_{-\infty}^{\infty} I^2(t)dt}_{modulated\ Spectrum} + \underbrace{2\int_{-\infty}^{\infty} I^2(t)dt}_{second\ Harmonic\ Spectrum} \\ & = 16\int_{-\infty}^{\infty} I^2(t)dt\end{aligned} \tag{13}$$

therefore, the ratio between perfect overlap and no overlap between the pulses corresponds to

$$\frac{\Gamma_{\text{IAC}}(\tau = 0)}{\Gamma_{\text{IAC}}(\tau = \pm\infty)} = \frac{16I^2}{2I^2} = \frac{8}{1} \tag{14}$$

The maximum peak-to-background ratio of an interferometric autocorrelation trace therefore is 8:1, the concept is displayed in Figure (2). The trace is symmetric, $\Gamma_{\text{IAC}}(\tau) = \Gamma_{\text{IAC}}(-\tau)$, which can be used to verify proper alignment. However, it should be noted that there are cases in which an asymmetric pulse will generate the same IAC trace as a symmetric one and there is no way to distinguish the two cases without deploying further characterization techniques [14]. Additionally, deviations from the theoretical 8:1 ratio can be attributed to a variety of factors; most commonly an imperfect ratio will be due to insufficient collinear alignment between the two beams, which can result in a substantially reduced peak-to-background ratio [17].
Furthermore, it is important to consider that a continuous wave (CW) laser source will not produce a 8:1 ratio but rather a 8:2 ratio, stemming from the fact that at for large delay times the light will still overlap, such that the I_{AC} term will always take on a value of 1, allowing the technique to be also used to make statements about whether a laser is mode-locked or not [17, 18].
By filtering out the fast oscillating terms I_ω, $I_{2\omega}$ (e.g. via electrical filters, a software algorithm performing a fourier transform or by simply using a detector with small enough bandwidth such that it averages out any fringes) the intensity autocorrelation trace can be retrieved, yielding the known peak-to-background ratio of 3:1. By further subtracting the background, the usual background-free intensity autocorrelation with peak-to-background ratio of 2:0 is obtained, from which a pulse

duration can be deduced by assuming a pulse shape; the most commonly used are Gaussian shaped pulses or solitons with a sech^2 pulse envelope.

2.2 Pulse Characterization

The following chapter provides a simple approach to make statements about pulse quality using the time-bandwidth product. The effect of chirp on the IAC trace is outlined and a mathematical description of a Gaussian pulse traveling through a fiber of known length and dispersive properties is given.

2.2.1 Time Bandwidth product

The Time-Bandwidth product of a pulse with pulse width τ_{P} and spectral bandwidth $\Delta\nu$ is given by:

$$TBP = \Delta\nu \cdot \tau_{\mathrm{P}} \tag{15}$$

It arises from the Fourier transform and highlights the uncertainty principle: Namely that there is a lower-bound in the temporal domain for a pulse for a given spectrum, i.e. it is not possible to compress a pulse to an arbitrarily small value without simultaneously increasing $\Delta\nu$ [14]. This in turn provides an upper limit for the maximum possible peak output power of a laser pulse for a given P_{avg}.

A pulse is transform-limited if it reaches its lowest possible TBP value for a given pulse duration and spectrum. For sech^2-shaped pulses, the lower limit is given by TBP = 0.315, while for Gaussian pulses it is TBP = 0.44 [14]. Deviations from the transform-limited value can arise due to dispersive effects, such as chromatic dispersion and different types of optical nonlinearities in the case of high power laser systems. For low-power laser systems, the contribution to pulse width shaping due to nonlinear effects is typically small such that it can be neglected. Dispersion will temporarily broaden the pulse, i.e. τ_{P} will increase, while the spectrum $\Delta\nu$ is kept constant. From equation (15) we can see that such a process will steadily increase the TBP, making the TBP an appropriate quantity to estimate the quality the laser pulses.

2.2.2 Pulse Quality & Chirp

Non-transform-limited pulses will exhibit chirp, which can be attributed to the fact that different frequency components of a pulsed laser will travel at different velocities through a medium, a process that is governed by the wavelength-dependent refractive index $n = n(\lambda)$. This effect will cause the pulse to be stretched out or compressed in the time-domain, depending on the dispersion regime the pulse travels through: normal dispersion will cause the pulse to be positively chirped, whereas anomalous dispersion produces negatively chirped pulses.

We can calculate the effect of a chirped Gaussian pulse on the IAC trace analytically. For this, the chirp parameter β is introduced, such that we can mathematically model the envelope of the electric field $E(t) = A(t) \cdot e^{i\omega t}$ by

$$A(t) = \exp\left(-\frac{1}{2}\frac{t}{\tau_{\mathrm{P}}}\right)^{2(1+i\beta)}$$

Plugging this into equation (5), we can determine the background-corrected IAC trace for a chirped pulse [14], which is given by

$$\Gamma_{\mathrm{IAC}}(\tau) = 1 + \left(2 + \exp\left(-\frac{\beta^2}{2}\left(\frac{\tau}{\tau_{\mathrm{P}}}\right)^2\right)\cos(2\omega t)\right)\exp\left(-\frac{1}{2}\left(\frac{\tau}{\tau_{\mathrm{P}}}\right)^2\right)$$
$$+ 4\exp\left(-\frac{3+\beta^2}{8}\left(\frac{\tau}{\tau_{\mathrm{P}}}\right)^2\right)\cos\left(\frac{\beta}{4}\left(\frac{\tau}{\tau_{\mathrm{P}}}\right)^2\right)\cos(\omega t)$$

From this equation it is already possible to make some statements about different approaches of autocorrelation measurements: Namely, when we omit all terms containing oscillations ω, we obtain the intensity autocorrelation. As mentioned previously, in this case all terms containing the chirp parameter β will also drop out, meaning that the simple intensity autocorrelation will not provide any information about the magnitude of chirp in a pulse.
Furthermore, a pulse with non-zero group delay dispersion (GDD) will have its intensity autocorrelation more spread out and "wings" will start to appear - for very large GDD values, the interferometric trace is reduced to its intensity trace in the wings [19, 20]. This is due to the fact that interference fringes will only appear in the IAC trace whenever both pulses overlap coherently for a given spectrum [14], which gives theoretical limit for the pulse retrieval using the fringe-counting method. Nevertheless, the intensity autocorrelation will still be resolved and can be used to retrieve pulse duration. The concept is depicted in Figure (3)

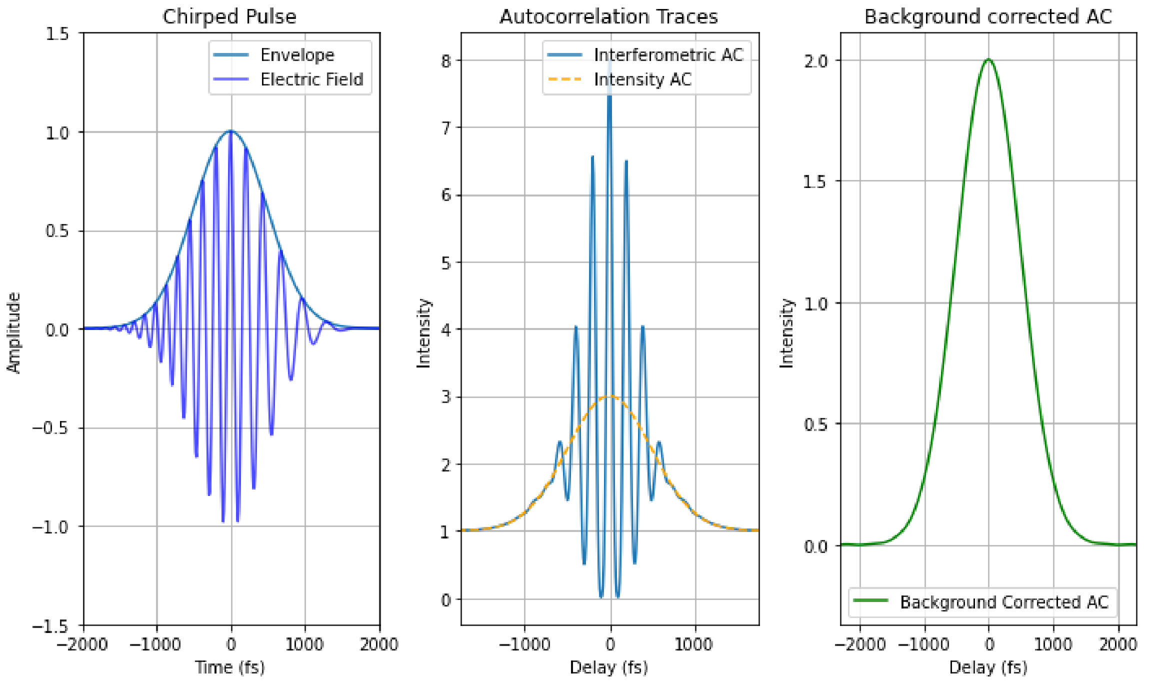

Figure 3: Effect of chirp on the interferometric autocorrelation trace. Left: chirped Gaussian pulse. Middle: Interferometric Autocorrelation and low-pass-filtered Intensity Autocorrelation of the chirped Gaussian pulse. The smearing out of fringes from the interferometric autocorrelation due to missing spectral coherence between the two beams can be seen in the form of wings, where the IAC trace "transitions" into the intensity autocorrelation. Right: Background-corrected intensity autocorrelation. Notice how the intensity autocorrelation yields the same result as in Figure (2), meaning that information about chirp is lost.

2.2.3 Light passing through a fiber

Pulsed laser light traveling through an optical medium will experience temporal broadening and chirping due to dispersion effects. The characterization of this effect can be modelled by two related parameters, namely group velocity dispersion (GVD) and GDD.

GVD quantifies how the group velocity v_g of a pulse varies with optical frequency ω. Its definition is given as the derivative of the inverse group velocity with respect to angular frequency:

$$\mathrm{GVD} = \frac{d}{d\omega}\left(\frac{1}{v_\mathrm{g}}\right) = \frac{d^2k}{d\omega^2} \tag{16}$$

with k as the wavenumber. GVD arises from the phenomenon that different frequencies of light will experience different refractive indices, such that the propagation speed through the medium is wavelength dependent via $c_\mathrm{n} = \frac{c}{n(\lambda)}$. The cumulative dispersion a pulse experiences when traveling through an optical element of length L is given by:

$$\mathrm{GDD} = \mathrm{GVD} \times L \tag{17}$$

Assuming that a Gaussian pulse with an initial FWHM pulse duration τ_0 travels through a fiber of length L, the pulse will experience broadening due to the dispersion. Neglecting other nonlinear effects such as self-phase modulation (which can be significant in high-intensity systems), the pulse duration τ_P when exiting the fiber is given by [21]:

$$\tau_\mathrm{P} = \tau_0 \cdot \sqrt{1 + \left(4 \ln 2 \cdot \frac{\mathrm{GDD}}{\tau_0^2}\right)^2} \tag{18}$$

This equation allows the retrieval of pulse duration after propagation through a dispersive element, given that the total GDD is known.

2.3 Nonlinear Polarization Optics for Harmonic Generation

Pulse width measurements require the detection of higher-order nonlinearities in order to quantify pulse duration; otherwise only the spectrum of the fundamental pulse is obtained. Commonly one uses a nonlinear crystal, which produces the second harmonic of the fundamental pulse, whose signal is then detected and typically amplified using a PMT.

The polarization response,$P(t)$, of a medium with non-zero nonlinear susceptibility of n-th order $\chi^{(n)}$ is given by [22]:

$$P(t) = \sum_n^\infty \epsilon_0 \chi^{(n)} E^n(t) = \epsilon_0[\chi^{(1)} E(t) + \chi^{(2)} E^2(t) + \chi^{(3)} E^3(t) + ...] \tag{19}$$

where the polarization $P(t)$ as well as the electric field were taken as scalar quantities for simplicity. $\chi^{(1)}$ describes linear absorption and refraction, the second order term, $\chi^{(2)}$ takes care of processes like second-harmonic generation, sum-frequency generation, and difference-frequency generation. $\chi^{(3)}$ is used to characterize third-order nonlinear processes, including the Kerr-Effect, Third-Harmonic Generation and 2-photon absorption, a special case of four-wave mixing. Second order processes can not occur in centrosymmetric media, as the $\chi^{(2)}$ vanishes for these types of material, while third-order processes can occur in both centro- as well as non-centrosymmetric materials [23].

The following chapter outlines the concepts for different types of nonlinear optical processes typically used in optical autocorrelators.

2.3.1 Second order nonlinear processes

Consider a laser source emitting light at two distinct frequencies, ω_1 and ω_2, the electric field can be expressed by

$$E(t) = E_1 e^{i\omega_1 t} + E_2 e^{i\omega_2 t} + E_1^* e^{-i\omega_1 t} + E_2^* e^{-i\omega_2 t} \tag{20}$$

The light is directed into a second-order nonlinear material, such that the change in polarization can be expressed by plugging in Equation (20) into Equation (19):

$$\begin{aligned} P^{(2)}(t) = \epsilon_0 \chi^{(2)} (&E_1^2 e^{-2i\omega_1 t} + E_2^2 e^{-2i\omega_2 t} \\ &+ 2E_1 E_2 e^{-i(\omega_1+\omega_2)t} + 2E_1 E_2^* e^{-i(\omega_1-\omega_2)t} \\ &+ c.c. + [E_1 E_1^* + E_2 E_2^*] \end{aligned} \tag{21}$$

where *c.c.* denotes the complex conjugate. Equation (21) can be rewritten as a sum over all frequencies ω_n:

$$\tilde{P}^{(2)}(t) = \sum_n P(\omega_n)e^{-i\omega_n t} \tag{22}$$

The complex amplitudes of the different frequency components are given by

$$\begin{aligned}\tilde{P}(0) &= 2\epsilon_0\chi^{(2)}E_1E_1^* + E_2E_2^* \\ \tilde{P}(2\omega_1) &= \epsilon_0\chi^{(2)}E_1 \\ \tilde{P}(2\omega_2) &= \epsilon_0\chi^{(2)}E_2 \\ \tilde{P}(\omega_1+\omega_2) &= 2\epsilon_0\chi^{(2)}E_1E_2 \\ \tilde{P}(\omega_1-\omega_2) &= 2\epsilon_0\chi^{(2)}E_1E_2^*\end{aligned} \tag{23}$$

The first expression describes Optical Rectification, whereas the $\tilde{P}(2\omega_1)$ and $\tilde{P}(2\omega_2)$ terms correspond to SHG. The terms $\tilde{P}(\omega_1+\omega_2)$ and $\tilde{P}(\omega_1-\omega_2)$ of equation 23 correspond to Sum- and Difference Frequency Generation respectively [22, 23].

2.3.2 Third order nonlinear processes

Considering now the effect of an optical field, oscillating at three different frequencies, ω_1, ω_2 and ω_3, such that

$$\begin{aligned}E(t) = {} & E_1e^{-i\omega_1 t} + E_2e^{-i\omega_2 t} + E_3e^{-i\omega_3 t} \\ & + E_1^*e^{i\omega_1 t} + E_2^*e^{i\omega_2 t} + E_3^*e^{i\omega_3 t}\end{aligned} \tag{24}$$

as they travel through third-order nonlinear medium. The change in third-order polarization is given by

$$P^{(3)}(t) = \epsilon_0\chi^{(3)}E^3(t) \tag{25}$$

Similar to the 2nd order case, the third-order polarization consists of an expression oscillating at 44 different frequencies [22] which are linear combinations of the individual input frequencies, describing different nonlinear processes, one of which is **Four-Wave mixing**, which describes the interaction between 4 individual electric fields [23]. **2PA** is a special case of four-wave mixing in which two of the waves are the same photon frequency such that the energy conservation of this process is expressed as $\chi^{(3)}(\omega_1 = \omega_1 + \omega_2 - \omega_2)$. Although the principle behind 2PA seems to be the very similar as for SHG, 2PA is a non-parametric process meaning the systems final state is real and the energy carried by the photons has been transferred to the semiconductor, whereas in SHG the final state is a virtual one since no absorption has taken place, "only" a new photon was generated. These third-order phenomena provide alternative approaches for pulse characterization, especially two-photon absorption, which will be discussed in detail in Chapter (2.4.2).

2.4 Semiconductor optics

Semiconductor optics is a field of study which deals with the interaction between light and semiconductor materials. Insight in how the transfer of energy happens as photons are absorbed linearly by the semiconductor is outlined in Chapter (2.4.1). When light intensities are large enough multi-photon transitions can occur, with the most common process being 2PA; a concept which is discussed in Chapter (2.4.2). Finally, the influence of different laser parameters, such as output power, spot size, pulse duration and repetition rate, on the induced 2PA current is discussed in Chapter (2.4.3).

2.4.1 Linear absorption

The response of a semiconductor to optical irradiation depends on the energy of a single incident photon, $h\nu$, as well as the bandgap energy, E_{BG}, of the semiconductor. In order for the semiconductor to be able to absorb the photon, the photon energy needs to be larger than the bandgap energy:

$$E_{\mathrm{Photon}} = h\nu > E_{\mathrm{BG}} \tag{26}$$

The absorption of a photon causes an electron to jump from the valence band into the conduction band, creating an electron-hole pair, allowing the charge-carriers to move freely under the influence of an external electric field, effectively generating a photocurrent $I_{\mathrm{Photocurrent}}$.

The probability for an incoming photon to excite an electron from the valence band into the conduction band is dependent on the quantum efficiency η of the process. η is defined as the fraction of the number of generated electron-hole pairs to the number of incident photons, which is related to the **spectral responsitivity** $\mathscr{R}$ of a photodiode via [24]

$$\mathscr{R} = \frac{\eta q}{h\nu} = \eta \frac{q\lambda}{hc} \tag{27}$$

where $\lambda = \frac{c}{\nu}$ is the wavelength of a single photon and $q = 1.602 \cdot 10^{-19}$ C, is the elementary charge.

The current generated by the free-moving electron-hole pairs depends on the number of photons reaching the photosensitive depletion region of the detector, the absorption coefficient α of the material as well as the fraction of electron-hole pairs that do not recombine right away.

The exponential decay in optical intensity as light travels through an absorptive medium of thickness z is described by the Beer–Lambert law

$$I(z) = I(0)e^{-\alpha z} \tag{28}$$

With α as the linear absorption coefficient in units [1/m]. The reciprocal value of α gives the absorption length, which is the penetration depth at which the intensity has dropped to $1/e$ of its original value.

2.4.2 Nonlinear Multi-Photon Absorption

When a photodiode is illuminated by a laser whose single photon energy is smaller than the bandgap energy of the semiconductor, $E_{\mathrm{Photon}} < E_{\mathrm{BG}}$ there will be no linear response as the photon energy is not large enough to excite the electron to the conduction band. However, there is a probability that the photon excites the electron into a quantum mechanical virtual state lying below E_{BG}. If a second photon with an appropriate energy such that $E_{\mathrm{Photon}} \approx E_{\mathrm{BG}}/2$ arrives within the lifetime of this virtual state, it is possible that the electron gets elevated into the excited state by absorbing both photons quasi-simultaneously. The theoretical basis of this effect was first described in the

1930s by Maria Goeppert-Mayer [2].
The energy bandgap condition for general n-photon absorption is given by

$$\frac{E_{\mathrm{BG}}}{n} < E_{\mathrm{Photon}} < \frac{E_{\mathrm{BG}}}{n-1} \tag{29}$$

where n is the number of simultaneously absorbed photons. With increasing number of interacting photons n, the required energy per photon decreases, yet the probability of all photons being absorbed simultaneously decreases.
The most likely n-absorption mechanism is given by 2-photon absorption, where $n = 2$:

$$\frac{E_{\mathrm{BG}}}{2} < E_{\mathrm{Photon}} < E_{\mathrm{BG}} \tag{30}$$

Consequently, for $n = 3$, the 3PA bandgap condition is given by

$$\frac{E_{\mathrm{BG}}}{3} < E_{\mathrm{Photon}} < \frac{E_{\mathrm{BG}}}{2} \tag{31}$$

A list of commonly used semiconductors as well as their 2-photon and 3-photon absorption range as given by the bandgap condition is shown in Figure (4)

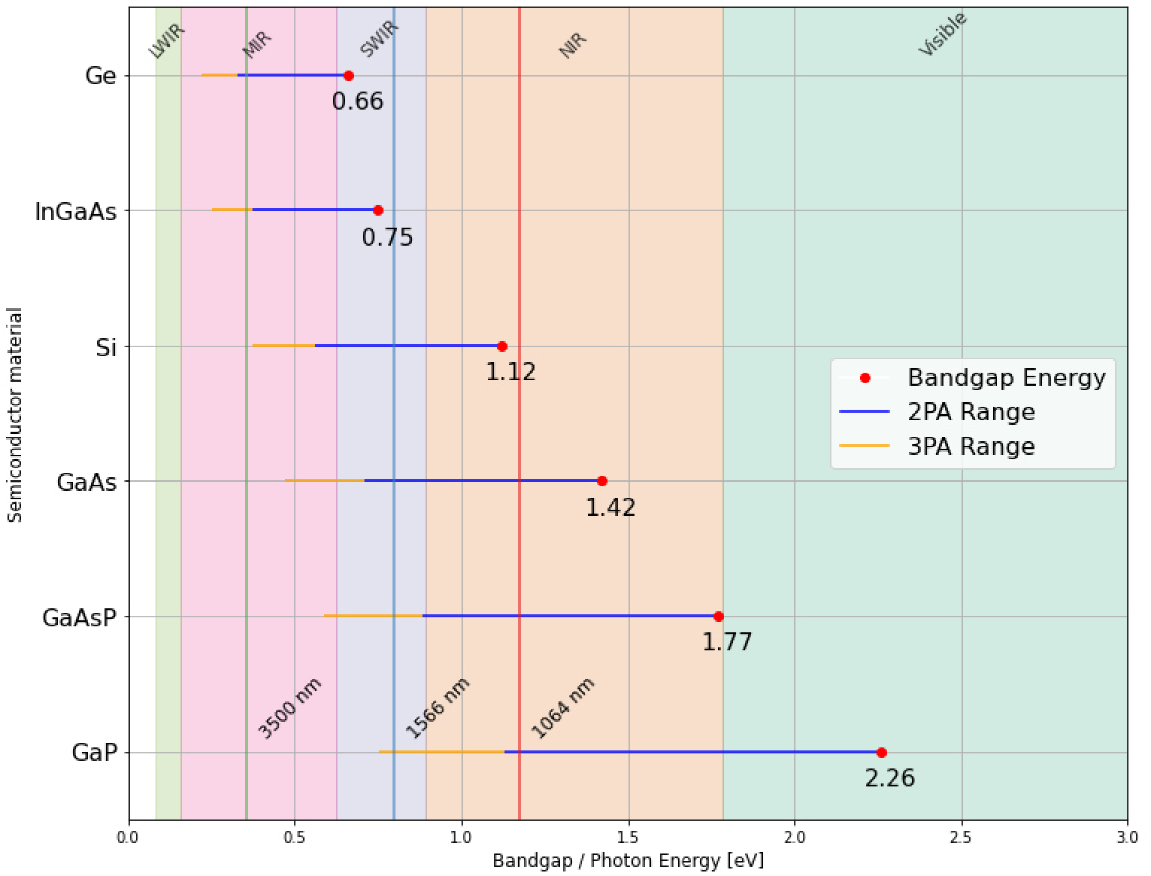

Figure 4: 2PA and 3PA ranges of commonly used semiconductors. Vertical lines indicate the single photon energy of the laser systems to be measured. The blue and orange lines indicate the energy range at which 2PA and 3PA can occur. The red dot represents the semiconductors bandgap energy, above which only linear absorption takes place.

The change in optical intensity I due to nonlinear absorption processes of order N when light travels through a medium is given by [23]:

$$\frac{dI}{dz} = \sum_{n=1}^{N} -\alpha^{(n)} I^n = -\alpha^{(1)} I - \alpha^{(2)} I^2 - \alpha^{(3)} I^3 - ... \tag{32}$$

where $\alpha^{(n)}$ describes the n-photon absorption coefficient. Since each coefficient $\alpha^{(n)}$ is directly proportional the $n-th$ power of the optical intensity, linear absorption will dominate for laser systems with small intensities.
Consequently, by focusing all the optical power into a small spot size, higher-order nonlinear absorption processes will start to dominate over linear absorption. Additionally, since the n-photon absorption coefficients $\alpha^{(n)}$ depend on the wavelength of the incident light, $\alpha^{(n)}(\lambda)$, it is possible to choose the semiconductor material in a way such that one can neglect all terms that do not

correspond to the desired n-photon absorption wavelength range. In the case of $n = 2$, contributions from all terms other than $n = 2$ are omitted, simplifying equation 32 to

$$\frac{dI}{dz} = -\alpha^{(2)}(\lambda)I^2 \tag{33}$$

The solution to this equation gives the change in optical intensity due to 2PA as light travels through an absorptive medium [25]:

$$I(z) = \frac{I_0}{1 + \alpha^{(2)} I_0 \cdot z} \approx I_0(1 - \alpha^{(2)} I_0 z) \tag{34}$$

allowing the retrieval of the number of photons absorbed in the active layer of thickness z of the photodiode. In typical photodiodes, the absorption depth is on the order of ≈ 1 µm. Plugging in typical values $\alpha^{(2)} \approx 10^{-11}$ m/W and peak intensities $I \approx 10^{12}$ W/m^2, the theoretically calculated number of electron-hole pairs created is about 10^{-4} per incident photon.

2.4.2.1 Lifetime and degeneracy of 2PA state

2PA is a quantum process where a photon is absorbed from the ground state $|g\rangle$ into a virtual energy state $|v\rangle$ lying in the classically forbidden band. The process is sketched in Figure (5). Depending on the energies of the incident photons, we differentiate between degenerate 2PA, where both photons have the same frequency, $\nu_1 = \nu_2$, and non-degenerate 2PA when the single photon frequencies have different values $\nu_1 \neq \nu_2$ but their energies still add up to the bandgap energy, $h\nu_1 + h\nu_2 = E_{\mathrm{BG}}$. The lifetime of this elevated virtual state $|v\rangle$ can be estimated via the Heisenberg uncertainty relation:

$$\Delta E \Delta t \geq \frac{\hbar}{2} \tag{35}$$

Since for degenerate 2PA, ΔE corresponds to half the bandgap energy (which in this case is also the single photon energy $h\nu = E_{\mathrm{BG}}/2 = \Delta E$) the lifetime can be estimated by $\Delta t \geq \frac{\hbar}{\Delta E} = \frac{1}{2\pi\nu}$. Given that a second photon with appropriate energy $E_{\mathrm{Photon}} \approx \Delta E$ arrives within the time Δt, both photons are absorbed simultaneously.

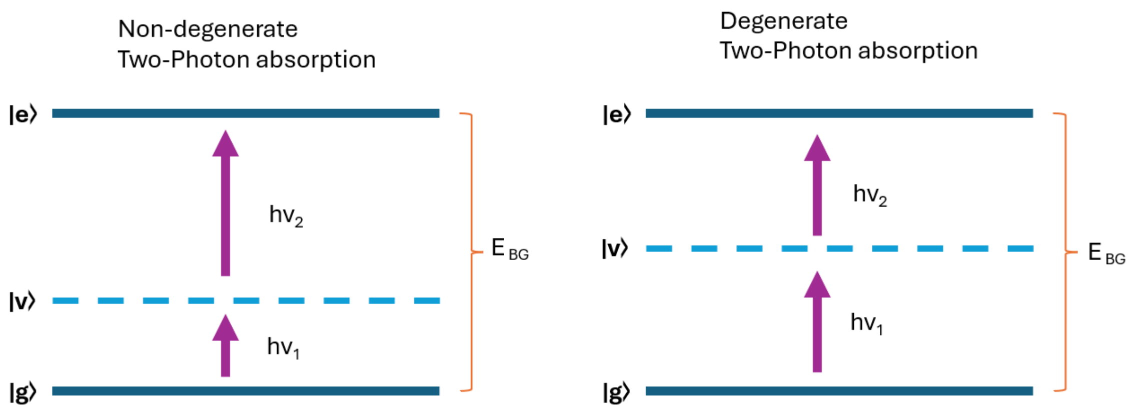

Figure 5: Concept of 2PA: The photon which arrives first excites the electron from the ground state $|g\rangle$ into the virtual state $|v\rangle$ which lies at approximately half the bandgap energy for the degenerate case. Given that a second photon arrives within the lifetime of the virtual state, the electron gets elevated to the excited state $|e\rangle$. If the two arriving photons have strongly different energies, 2PA can still occur, but the probability decreases with increasing energy of the first photon, as in this case, the lifetime of the virtual state also decreases.

Typical bandgap energies for commercially used semiconductors in photodiodes range from ≈ 0.5 eV to ≈ 5 eV, yielding lifetimes of a 2PA virtual state of $\Delta t \geq \frac{\hbar}{E_{\mathrm{BG}}} \approx 1$ fs.

2.4.2.2 Bandgap dependence of 2PA coefficient

One usually differentiates between direct and indirect bandgap transitions when an electron jumps from the valence band to the conduction band. If the k-vector changes when jumping from the lower to the higher state, the bandgap transition is considered indirect, as another particle (e.g. phonon) is present during the process. The semiconductors crystal structure determines whether this is required; direct bandgap semiconductors include Indium Arsenide, Gallium Arsenide, while indirect semiconductors include Germanium and crystalline Silicon. Due to the required assistance of a phonon, indirect bandgap transitions are typically harder to detect as some of the absorbed energy is dissipated as heat [26].

Theory predicts that the 2PA coefficient for a given incident wavelength scales as $\frac{1}{E_{\mathrm{BG}}{}^3}$ [27]. This has been verified experimentally [28, 29] and has shown excellent agreement for an extensive range of wavelengths, reaching from the visible to the infrared as well as bandgap energies E_{BG} from 0.18 eV (Indium antimonide) to 3.66 eV (Zinc Selenide) [30, 27]. The 2PA coefficient for Silicon has been experimentally measured several times, with values between 2 cm/GW to 0.45 cm/GW [31, 32, 33]. The dependence of the 2PA coefficient on bandgap and single photon energy $h\nu$ can be expressed as [34]:

$$\alpha^{(2)} = K^{(2)} \frac{\sqrt{E_{\mathrm{p}}}}{n^2 E_{\mathrm{BG}}{}^3} \frac{(\frac{2h\nu}{E_{\mathrm{BG}}} - 1)^{3/2}}{(\frac{2h\nu}{E_{\mathrm{BG}}})^5} \tag{36}$$

Where $K^{(2)}$ describes a material-independent constant having an approximate value of $3.1 \frac{eV^{5/2}cm}{MW}$,

E_p is the Kane energy, which is usually taken to be material-independent, with most commercially available semiconductors having a typical value of around 20 - 25 eV [28]. n is the refractive index of the semiconductor material. The dependence of the 2PA coefficient on incoming photon energies as predicted by equation (36) is plotted in Figure (6), for a set of commonly used semiconductors. For simplicity, the refractive index is taken to be wavelength independent, $n(\lambda) = n$.

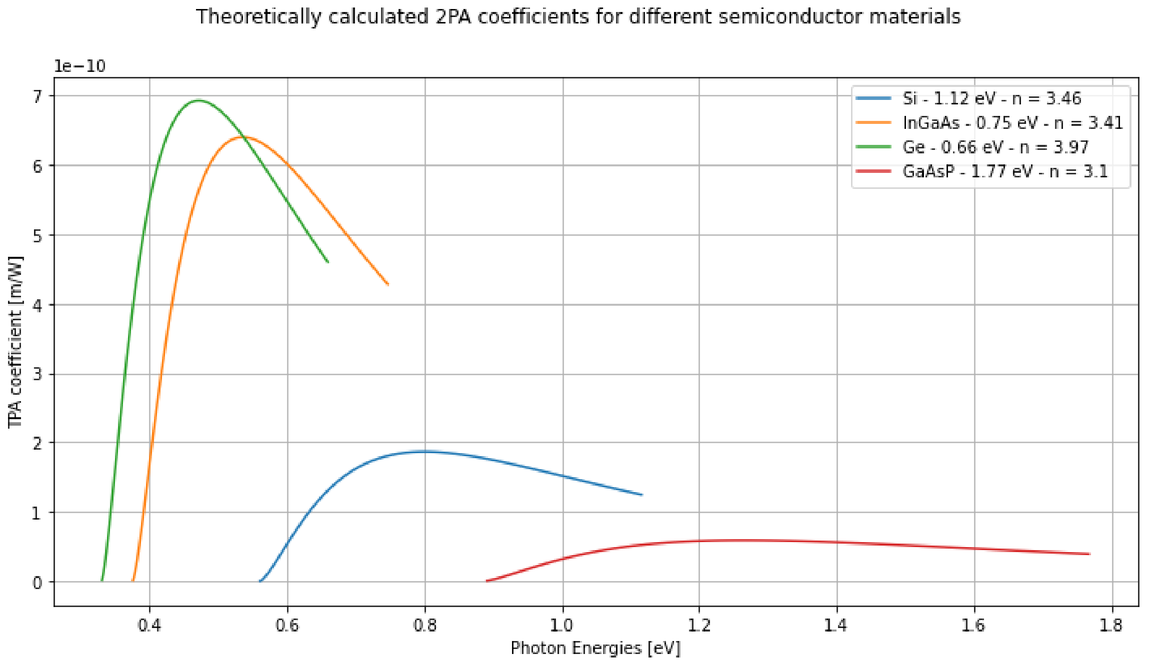

Figure 6: Theoretical values for the two photon absorption coefficient of typically used semiconductors, calculated via Garcia bandgap scaling theory

From Figure (6) one can see that the efficiency of the 2PA process depends strongly on the incoming photon energy. Typically a peak is reached at half the bandgap energy, followed by a relatively flat drop-off before the bandgap condition allows for the linear absorption mechanism to become more dominant.

2.4.3 Induced 2PA Photocurrent

The next chapter will provide information about the influence of spot size, average and peak laser power as well as pulse duration of the incident light on the efficiency of the 2PA process. For this, we consider a laser with average energy P_avg and center frequency ν striking a semiconductor material whose bandgap energy is suitable for 2PA. The photon flux Φ, representing the number of photons impinging onto the semiconductor each second is given by:

$$\Phi = \frac{dN_\mathrm{Photon}}{dt} = \frac{P_\mathrm{avg}}{h\nu} \tag{37}$$

The induced 2PA current in the photodiode depends on various parameters: The optical intensity dictates how much light is present per unit area, i.e. the induced 2-photon current can be increased

either by increasing the number of photons striking the photodetector (increased average power) or by decreasing the spot size, accommodating more photons within the same area. Additionally, shorter **pulse widths** and therefore larger peak powers increase the induced current by increasing the probability that a second photon arrives within the lifetime of the virtual state as outlined in chapter 2.4.2.1.
The induced current can be estimated via the following Equation [25]:

$$I_{\text{Photocurrent}} = \eta\alpha^{(2)}\frac{q}{h\nu}zA\frac{{P_{\text{avg}}}^2}{\omega_0^4\pi^2 \cdot \tau_{\text{P}} f_{\text{rep}}} \tag{38}$$

where η, z and $\alpha^{(2)}$ are the photodiodes internal efficiency at the 2PA wavelength, the thickness of the absorption layer of the photodiode and the 2PA coefficient of the semiconductor, respectively. Unless one aims to design the photodiode by oneself, the depth of the absorption layer is a fixed quantity given by the manufacturer and can therefore not be modified in order to increase the generated photocurrent. $\frac{q}{h\nu}$ acts the conversion factor between optical and electrical energy. τ_{P} is the pulse duration and f_{rep} the lasers repetition rate, A corresponds to the area illuminated by the laser. For the case that all laser light is contained within the active area of the photodiode, one can estimate $A \approx \omega_0^2\pi$, further simplifying the equation to

$$I_{\text{Photocurrent}} = \eta\alpha^{(2)}\frac{q}{h\nu}z\frac{{P_{\text{avg}}}^2}{\omega_0^2\pi \cdot \tau_{\text{P}} f_{\text{rep}}} \tag{39}$$

which can be rewritten to express the induced current as a function of the average optical intensity $I_{0,\text{avg}}$ in W/m^2:

$$I_{\text{Photocurrent}} = \eta\alpha^{(2)}\frac{q}{h\nu}zA\frac{{I_{0,\text{avg}}}^2}{\tau_{\text{P}} f_{\text{rep}}} \tag{40}$$

The peak intensity can be estimated for a given repetition rate and assumed pulse duration via

$$I_{0,\text{Peak}} = \frac{I_{0,\text{avg}}}{f_{\text{rep}} \cdot \tau_{\text{P}}} = \frac{P_{\text{avg}}}{\omega_0^2\pi \cdot \tau_{\text{P}} f_{\text{rep}}} \tag{41}$$

allowing us to rewrite equation (39) as

$$I_{\text{Photocurrent}} = \eta\alpha^{(2)}\frac{q}{h\nu}zA{I^2}_{0,\text{Peak}}\tau_{\text{P}} f_{\text{rep}} \tag{42}$$

Input power dependence of 2PA
The induced current depends on the conversion efficiency of the 2PA process. Higher average input power directly translates to more photons being present per pulse. Equation (39) indicates that the value of the induced 2PA current scales as $I_{\text{Photocurrent}} \propto {P_{\text{avg}}}^2$ [15].

Spot size dependence of 2PA
A smaller spot size of a laser pulse translates to a higher number of photons hitting within the same area of the semiconductor, making 2PA more likely. Ideally all of the spot size is contained within the detectors active area. In this case, one can see from equation (39), that the induced 2PA photocurrent scales as $\frac{1}{\omega_0^2}$, making the spot size the easiest-to-manipulate parameter for 2PA experiments.
A beam with wavelength λ hitting a lens with focal length f will result in a focal spot size $2\omega_0$ given by [22]

$$2\omega_0 = \frac{4\lambda M^2 f}{\pi D} \tag{43}$$

where M^2 is the beam quality factor, for which we will assume a perfect gaussian beam, i.e. $M^2 = 1$. The input beam diameter D is dictated by the used collimator, enabling us to optimize the process either by increasing the input beam diameter or by using a lens with a small focal length.

Pulse duration dependence of 2PA

2PA is a quantum mechanical process that relies on the Heisenberg uncertainty relation, as outlined in chapter (2.4.2.1). The pulse duration of the individual laser pulses affect the efficiency of the 2PA process. Once the first photon has been absorbed to the virtual state, a second photon needs to arrive within $\approx 1fs$ in order to generate a 2-photon signal. By squeezing the same number of photons into a shorter pulse duration, the number of photons arriving while the first photon is in its virtual state increases, therefore increasing the processes efficiency. From equation (39) one can see that the induced current scales as $I_{\text{Photocurrent}} \propto \tau_{\text{P}}{}^{-1}$, providing a handle on the 2PA efficiency by the use of e.g. a grating compressor to adjust the pulse length.

2.5 Photodetector

Photodiodes consist of a doped semiconductor material where one side is positively charged (p-type) and the other is negatively charged (n-type). This charge gradient creates an electric field across the photodiode, causing flow of positively charged holes to the n-type region and negatively charged electrons to the p-type region, resulting in a region without free carriers. This carrier-free region is known as the **depletion region** of the photodiode and the electric field across it is the photodiodes **built-in voltage**.
The size of the depletion region of a photodiode can be modified by applying an external voltage bias. Depending on the polarity of the applied voltage, one differentiates between forward biasing, where the photodiode is operated in photovoltaic mode, and reverse biasing, where the photodiode is operated in photoconductive mode.
In **forward biased operation**, the externally applied voltage causes the depletion region to get narrower. By applying the negative polarity to the p-type region of the semiconductor and vice versa, the photodiode is operated in **reverse bias**, increasing the built-in voltage and widening the depletion region. This directly improves the speed of response and linearity of the photodiode, with the downside of also increasing the dark current generated by the diode.
The photodiode equivalent circuit model as pictured in Figure (7) splits a photodiode into individual electrical components, allowing for a simpler characterization of a photodiodes electric behavior.

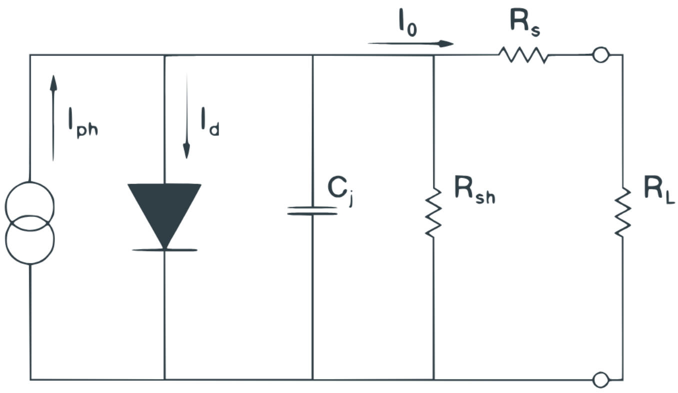

Figure 7: Photodiode equivalent circuit model

When a photon hits the active area of the photodiode, a photocurrent is generated, depending on the photodiodes spectral response to the wavelength of the incoming photon. However, due to the built-in electric field across the diode, there is a charge carrier drift (electrons moving from n-side to p-side and holes moving from p-side to n-side), which also generates an unwanted **dark current**, I_{Dark}, to the output current of the photodiode.

$$I_{\mathrm{out}} = I_{\mathrm{Photocurrent}} + I_{\mathrm{Dark}} \tag{44}$$

The **Shunt resistance**, R_{Sh}, is the resistance placed in parallel to the photodiode. Ideally, the shunt resistance has a value of infinity, as in this case all of the generated current is transferred to the load resistance and a direct current-to-voltage conversion is possible. The more R_{Sh} deviates from its ideal value of ∞, the higher is its contribution to the Johnson noise and the more generated current is redirected across R_{Sh}, influencing the diodes' current-to-voltage conversion. Typical, commercially available photodiodes have values of $R_{\mathrm{Sh}} \gg 1$ MΩ, so in good approximation it can be treated as virtually infinite.
The photodiodes depletion region acts as a parallel plate capacitor, whose junction capacitance is given by

$$C_{\mathrm{J}} = \frac{C_{\mathrm{J0}}}{\sqrt{1 + \frac{V_{\mathrm{R}}}{\Phi_{\mathrm{B}}}}} \tag{45}$$

The junction capacitance of the diode is also directly connected to the rise time, t_{r}, which is the time at which the signal has risen from 10 % to 90% of the final value. t_{r} is connected to the bandwidth f_{BW} via $t_{\mathrm{r}} \approx \frac{0.35}{f_{\mathrm{BW}}}$. The applied value of the reverse-bias can therefore be used to adjust the bandwidth of the detector:

$$f_{\mathrm{BW}} = \frac{1}{2\pi C_{\mathrm{J}} R_{\mathrm{L}}} \tag{46}$$

where R_{L} is the external **load resistance**, allowing for adjustment of the current-voltage gain setting via

$$V_{\mathrm{Out}} = I \cdot R_{\mathrm{L}} \cdot \mathscr{R} \tag{47}$$

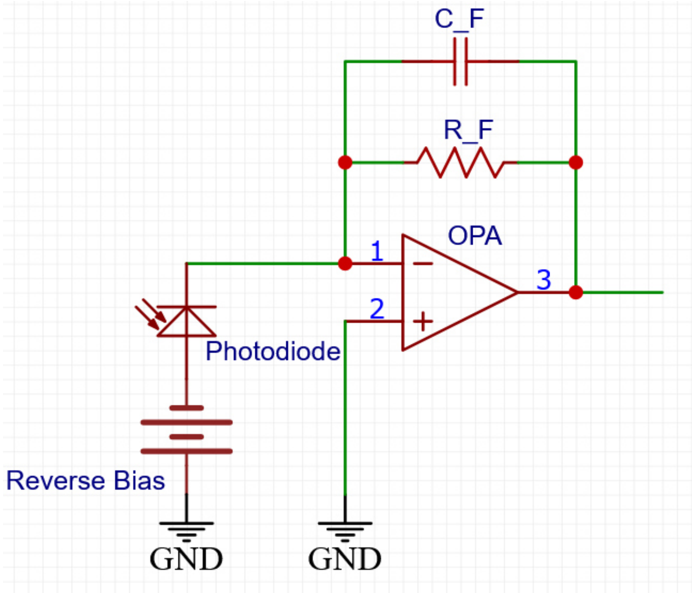

Figure 8: Basic scheme of a reverse biased photodiode with a transimpedance amplifier

where $\mathscr{R}$ describes the responsitivity of the diode as outlined in chapter (2.4.1). Finally, series resistance, R_S of a photodiode is the sum of all the resistance of the contacts and the resistance of the undepleted region. Although an ideal photodiode should have no series resistance, typical values are on the order of few 10s to 1000s of Ω [24], affecting the linearity of the photodiode.

2.5.1 Transimpedance Amplifier Design

As outlined in chapter (2.4.3), low-input power laser systems will generate 2PA photocurrents on the order of a few nA to low µA values. In order to measure and reliably resolve such a small current on a commercially available oscilloscope, an appropriate amplification mechanism has to be chosen. Generally, one uses a transimpedance amplifier as a current pre-amplifier, where the induced current is converted into a measurable voltage. Transimpedance amplifiers can be either bought commercially or home-built using an operational amplifier (OPA). The proper choice of the OPA is crucial, especially when working with low power laser systems, as the induced current will be very small and might get completely masked by the internal noise of the electrical components. The basic layout of an amplified photodetector is pictured in Figure (8). The OPA works by keeping voltages of the the non-inverting input (-, or 1 in Figure (8)) and the inverting input (+, or 2 in Figure (8)) equal, such that any current that is generated by the photodiode will flow through the feedback resistor R_F, transferring the small current to a voltage. The magnitude of amplification depends directly on the value of the R_F via Ohms law, $V_{out} = R_F \cdot I_{Photocurrent}$.

The applied gain directly limits the maximum possible bandwidth of the detector via the gain bandwidth product (GBP) of the OPA, determining the maximum possible gain value for a given desired bandwidth. Additionally, the input bias current I_{Bias} dictates the smallest possible current that can be distinguished from noise by the OPA, so the OPA should be chosen such that $I_{Photocurrent} \gg I_{Bias}$.

Choice of gain and feedback capacitor

Let I_{max} be the maximum expected current generated by the photodiode. Let $V_{\mathrm{out,max}}$ and $V_{\mathrm{out,min}}$ be the desired maximum and minimum output voltages to be displayed the signal analyzer. The gain factor shall then be chosen via the feedback resistor $\mathrm{R_F}$ such that:

$$R_{\mathrm{F}} = \frac{V_{\mathrm{out,max}} - V_{\mathrm{out,min}}}{I_{\mathrm{max}}} \tag{48}$$

To prevent signal distortion and maintain stable bandwidth, a feedback capacitor is placed parallel to the feedback resistor.

When choosing larger gain values, unwanted electrical oscillations will manifest themselves in the amplifier system. To prevent signal distortion and maintain stable bandwidth, a feedback capacitor is placed parallel to the feedback resistor, whose capacitance should not exceed:

$$C_{\mathrm{F}} < \frac{1}{2\pi f_{\mathrm{BW}} R_{\mathrm{F}}} \tag{49}$$

Choice of OPA

The OPA should be chosen according to two main parameters, namely the GBP as well as its input bias current I_{Bias}. In order to properly resolve the 2PA photocurrent, one should choose the OPA such that $I_{\mathrm{Photocurrent}} \gg I_{\mathrm{Bias}}$. The required GPB depends on the sum of the input capacitance of the photodiode, the differential input capacitance of the amplifier as well as the common-mode input capacitance of the inverting input; $C_{\mathrm{i}} = C_{\mathrm{Diode}} + C_{\mathrm{Differential}} + C_{\mathrm{CM}}$ as well as the two previously chosen feedback components via:

$$GBP > \frac{C_{\mathrm{i}} + C_{\mathrm{F}}}{2\pi R_{\mathrm{F}} {C_{\mathrm{F}}}^2} \tag{50}$$

3 Setup & Results

The following chapter provides information on how the autocorrelator system was arranged and the results that were obtained. Chapter (3.1) provides information on the setup of the Michelson-Interferometer, including the characterization of the delay stage and the used detectors. The first results related to general 2PA are given in Chapter (3.2). Pulse duration measurements and their analysis are provided in Chapter (3.3).

3.1 Autocorrelator Setup

The basic setup used in this work is a collinear Michelson-Interferometer configuration as depicted in Figure (9).

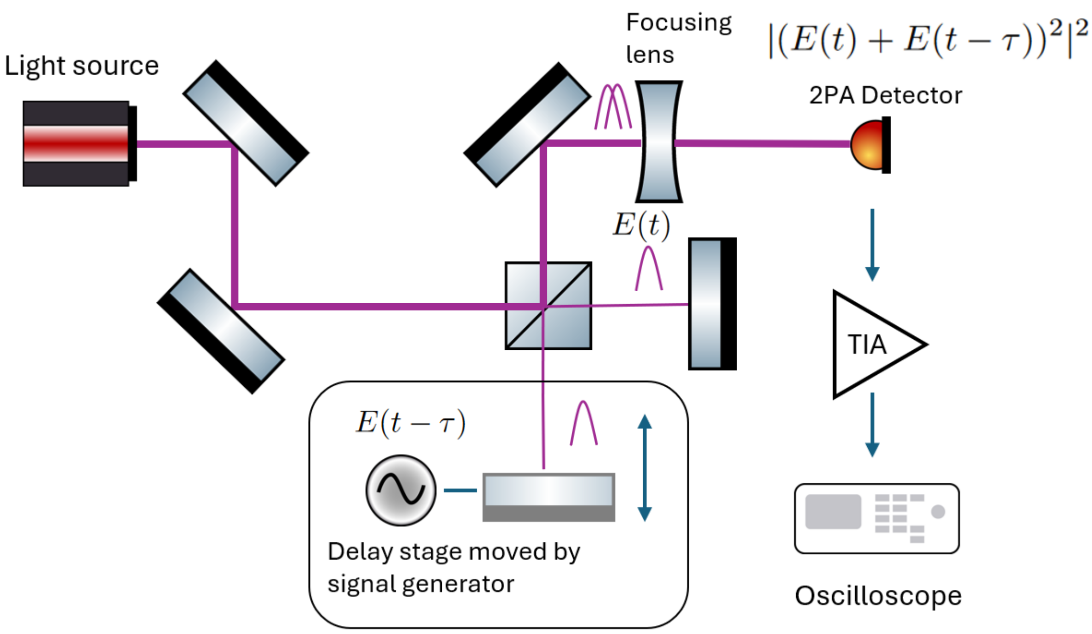

Figure 9: Collinear Michelson-Interferometer configuration for interferometric autocorrelation via 2PA. The delay stage moves through through a signal generator before the beams are recombined in the beam splitter and focused onto the nonlinear detector. The generated current is amplified using a transimpedance amplifier and then displayed on an oscilloscope.

The incoming electric field is split into two equal parts by a 50:50 beam splitter. The transmitted arm is reflected back into the beam splitter by a silver mirror. A mirror attached to a loudspeaker acts as the delay stage in the reflected arm. The loudspeaker is displaced using a signal generator outputting a sinusoidal wave and was chosen such that it shows adequate linear response to low-frequency electrical input signals in order to properly resolve the interferometric fringes. The recombined beams are tightly focused onto a photodiode selected for its 2PA spectral response.

In order to be able to move the detector through the focal plane of the system, the detector was mounted onto a translation stage as well.

The generated output current from the photodiode is amplified using a transimpedance amplifier. In principle, one should choose the first stage gain to be as large as possible since any noise contribution from the transimpedance amplifier will be further amplified by the second amplification stage.

In order to facilitate the alignment of the autocorrelation system, the 2PA detector is replaced by a linear detector first. The signal of the linear interferogram is maximized by adjusting the position of the delay-stage mirror via a translation stage and fine-tuning the angle of the reflected beam off the speaker mirror. In order to make sure that unwanted resonance effects of the mirror do not distort the IAC trace, the zero-path difference between the two pulses should be set to be in the linear displacement regime of the speaker. Additionally, one should ensure that the delay mirror reflects the beam back onto the same spot on the detector for maximum and minimum displacement of the speaker. The simplest way to do this is to move the translation stage all the way to the back, align the two beams back onto the beam splitter. Now the translation stage is moved all the way to the front and the beam is aligned once again. This process is iterated until the beam hits the same spot on the detector for all positions on the translation stage. Once the linear interferogram is maximized, the 2PA detector can be inserted. Since the nonlinear 2PA signal is maximized in the focal plane of the beam, the 2PA detector is mounted onto a translation stage and a Z-Scan measurement is performed to extract the exact position of the focal plane and verify symmetric alignment.

3.1.1 Calibration of delay stage and pulse duration retrieval

Two different methods exist which allow the retrieval of pulse duration. The simpler "fringe-counting method" requires only knowledge of the fundamental wavelength of the incoming pulse, while the typically, field-deployed intensity autocorrelation method requires additional characterization and calibration of the delay stage. As for the fringe-counting method, let N be the number of fringes in the FWHM of the IAC trace, then the pulse width of the autocorrelation signal is given by [35]:

$$\tau_{\mathrm{P}} = \frac{N\lambda}{c} \tag{51}$$

Where λ is the wavelength of the fundamental beam. For a known temporal pulse shape, the pulse duration is then given by the deconvolution factor multiplied by the FWHM of the autocorrelation signal. The deconvolution factor for Gaussian-shaped pulses is 0.707, for sech^2-shaped pulses, it is given by 0.647. It arises from the mathematical relationship between the pulses temporal profile and its autocorrelation function [36]. Imperfect peak-to-background ratios will change the full-width half maximum and will therefore wrongly estimate the pulse duration. Such imperfections are typically the result of misalignment, either due to the beams not overlapping perfectly in collinear way or due to the input beam entering the autocorrelator at an imperfect angle [37]. Nevertheless, even at an imperfect peak-to-background ratio, the real FWHM pulse duration will not deviate from the misaligned pulse duration by more than a factor of 2 [17].

In case that the fringes cannot be resolved (e.g. due to a low bandwidth detector), the intensity autocorrelation can be used to deduce the pulse duration, requiring additional calibration of the autocorrelators delay stage. The spatial displacement at any given time τ of the delay stage is governed by the voltage applied by the signal generator – it acts as the conversion to the true time step via

$$\Delta t_{\mathrm{true}} = \frac{2\Delta d}{c} \tag{52}$$

with Δd as the spatial delay step. When saving data using an oscilloscope (Keysight DSOX3024T) and given that the velocity and total displacement of the delay stage mirror is known, the temporal distance between two saved datapoints can be calculated the following way:
Let v_{m} be the velocity of the mirror such that $d_{\mathrm{total}} = v_{\mathrm{m}} \cdot t_{\mathrm{total}}$ is the distance covered by the delay stage in time t_{total} in a full cycle and let N be the number of datapoints sampled from the interferogram. The temporal distance between two datapoints Δt in the saved data is calculated via

$$\Delta t = \frac{1}{N} \cdot \frac{v_{\mathrm{m}}\ t_{\mathrm{total}}}{c} \tag{53}$$

which is then used to extract the true pulse duration from the obtained intensity autocorrelation trace, once again, after application of the deconvolution factor.
The calibration of the autocorrelators delay stage was performed using a continuous wave laser emitting at $\lambda = 632$ nm for applied voltages ranging from 1V to 16V. The number of fringes was counted each time and multiplied by $\lambda/2$ to obtain the spatial displacement d for a full cycle of the loudspeaker. The velocity of the mirror v_{m} can then be obtained by multiplying the displacement with the frequency applied by the signal generator. The displacement of the delay stage over a whole cycle as a function of the applied voltage is listed in Table (1):

Voltage	# of fringes	Total Displacement [mm]
1	71	0.022436
2	174	0.07134
6	479	0.151364
12	984	0.310944
16	1384	0.437344

Table 1: Displacement of the delay stage for varying speaker voltages during sinusoidal cycles measured using a 632 nm CW calibration laser.

Since an applied voltage of 16 V offered the largest displacement without risking damage to the speaker mirror, this value was chosen for most measurements, corresponding to a maximum mirror displacement of $d_{max} \approx 0.219$ mm for a single interferogram. This value also provides the upper limit of a possible pulse duration measurement of ≈ 1.3 ps.
However, due to the fact that the delay stage is driven by a sinusoidal signal, the available autocorrelation scanning range is restricted to the region where the loudspeakers displacement remains linear. As one approaches the turnaround points of the loudspeaker motion (corresponding to the maximum and minimum of the applied voltage), the delay stages displacement deviates from its linear relationship, causing a tendency to distort the IAC trace.
In order to quantify the range of the linear regime, the same 632 nm calibration laser was used and the distance between two consecutive interference fringes were examined. As a measure of linearity, we introduce the coefficient of variation $CV = \frac{\sigma}{\mu}$, with μ as the average distance between two interference peaks and σ as its standard deviation. A perfectly linear motion would produce equal spacing between two interference maxima, which yields $CV = 0$, while any deviation from this value indicates that the loudspeaker starts to accelerate.
The CV value for the whole sinusoidal half-cycle was found to be 0.42, indicating that not the full delay line could be used for autocorrelation measurements. By incrementally removing the outermost fringes (and therefore reducing the maximum pulse duration that can be reliably measured),

the CV factor gradually decreased, indicating that the movement became more linear. The concept is depicted in Figure (10). The trade off between linearity and autocorrelation scan range was chosen to be 5 % deviation from linearity, which was retrieved to be 310 ± 5 fringes, corresponding to a displacement of 0.098 mm, or $\approx$ 45 % of the sinusoidal half cycle, limiting the autocorrelation scanning range to $\approx$ 650 fs. Although the fringes of slightly longer pulses can still be resolved, the nonlinear motion of the delay stage will cause the autocorrelation pulse duration to be distorted, introducing systematic error when retrieving the pulse duration.

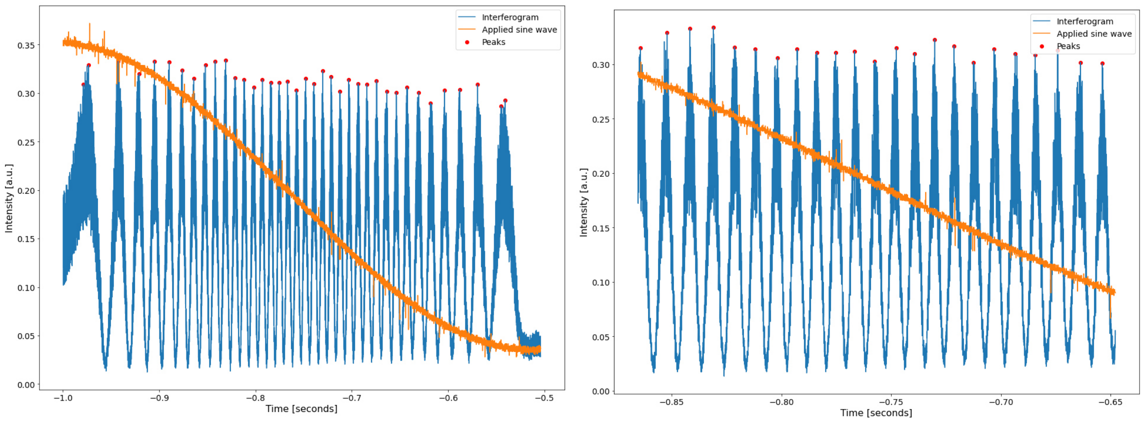

Figure 10: Removal of outermost fringes at the turnaround point of the delay stage to isolate the linear regime of the delay stage. Left: A sinusoidal half cycle, with the interference peaks marked in red. Notice how the spacing of interference fringes becomes larger at the turnaround points of the mirror, indicating that the motion is not anymore linear. Right: First iteration of removal of outermost fringes. Procedure is repeated until the CV factor corresponds to less than 5% deviation from linearity. Note: The applied voltage was chosen to be 1 V to better depict the concept.

As a quick double check for proper calibration of the autocorrelator, the pulse durations obtained from the fringe-counting method and the intensity autocorrelation method should be within measurement error.

3.1.2 Photodetector & Amplifier

For the Yb laser system, a GaAsP photodiode (Hamamatsu G1115) was reverse-biased at 3.3 V. The generated photocurrent was amplified using a Texas Instruments OPA828 as the base for the TIA. The peak one-photon response of the photodiode was 0.3 A/W for $\lambda = 600$ nm and about 0.25 A/W of linear response at $\lambda \approx 520$ nm, which corresponds to half the wavelength of the system to be investigated. Unfortunately, even though the theoretical current should be on a similar order of magnitude as the measurements for the Er-DC system, a peak 2PA photocurrent of only 32 nA was measured for the highest possible power hitting onto the detector (15 mW). At this point, the use of a 1 MΩ feedback resistor was required, therefore severely reducing the bandwidth of the detector to only 45 Hz. Electrical oscillations were prevented by choosing an appropriate feedback capacitor C_{F} = 3.3 nF, the closest value to the theoretically required 3.53 nF. The electrical layout of the used TIA is pictured in Figure (11), an in-depth noise analysis of the circuit is provided in Appendix (A).

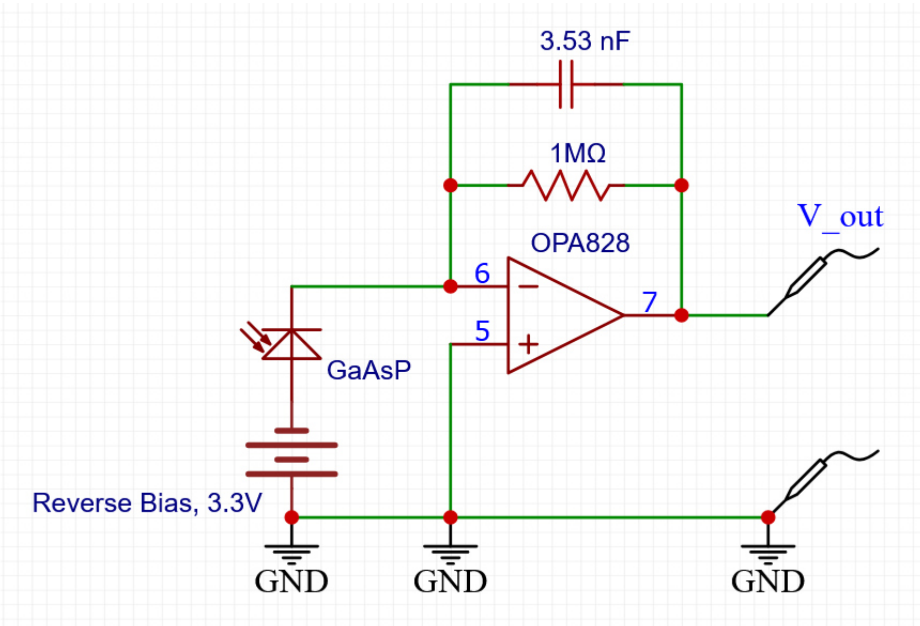

Figure 11: Reverse-biased GaAsP photodiode with transimpedance amplifier with a gain of 120 dB.

For the Er-DC measurements, a commercially available switchable-gain photodetector (Thorlabs PDA36A) at the maximum gain setting of 70 dB (corresponding to a TIA gain of $1.5 \cdot 10^6$ V/A) was used, which had a much larger bandwidth (3.5 kHz) than the home-built TIA, which allows for higher scanning frequency (up to 10 Hz) applied to the delay stage without losing the ability to resolve the individual fringes of the interferogram, even at large displacements of the delay stage mirror.

As for the GaAsP detector measuring the Yb-NALM system, the voltage applied to the delay stage was 16 V; as for the applied frequency, a variety of values was tested - a clear resolution of the fringes without drowning them out by electrical noise of the detector was achieved by using values < 50 mHz, indicating scanning times of 20 seconds for a single interferogram - a downside that was observed by other publications already [38]. In general, the SNR of the IAC traces got better as the velocities of the delay stages were reduced.

3.2 2PA Results

3.2.1 Dependence of induced 2PA current on average input power

In order to quantify the induced 2PA current in silicon at $\lambda_{\text{center}} = 1.57$ µm as a function of average power onto the photodiode, a $\lambda/2$-waveplate and a polarizing beam splitter were inserted before the detector, allowing to modify the power impinging onto the detector by simply changing the angle of the waveplate. The maximum voltage reading was then divided by the transimpedance gain of $1.5 \cdot 10^6$ V/A to obtain the induced 2PA current. The same dependence was also investigated for the homemade GaAsP Photodetector, which amplified the current by a factor of 10^7 V/A. Both results are shown in Figure (12). The experimentally obtained datapoints were fitted to a power law and yield a slope of 1.907 in the log-log scale for the Er-DC system and a slope of 1.891 for the Yb-NALM system, indicating that the absorption processes can be attributed to 2-photon absorption.

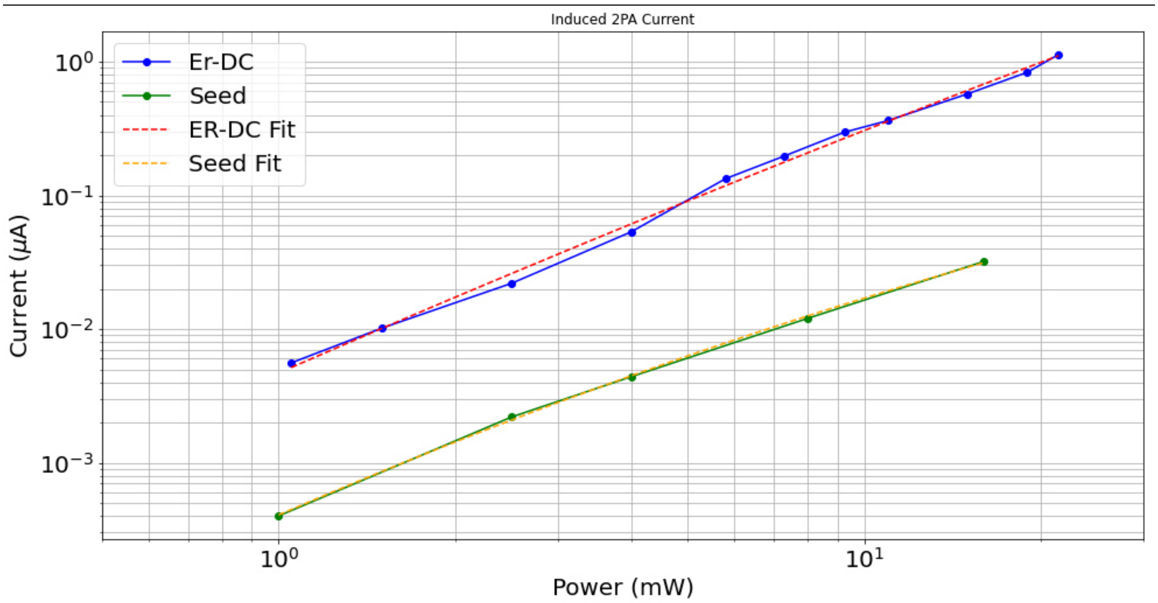

Figure 12: Induced 2PA currents of the Er-DC in Silicon photodiode and the Seed laser using a GaAsP photodiode as a function of the average power impinging onto the detector. A quadratic fit was deployed and a slope of 1.907 was retrieved for the Er-DC system and 1.891 for the NALM system in the log-log scale, indicating that the absorption process was due to 2PA.

3.2.2 Z-Scan

In order to quantify the induced 2PA current as a dependence on the focal spot sizes, open-aperture Z-scan measurements were performed for both systems. They measurements are plotted in Figure (13) and Figure (14) respectively.

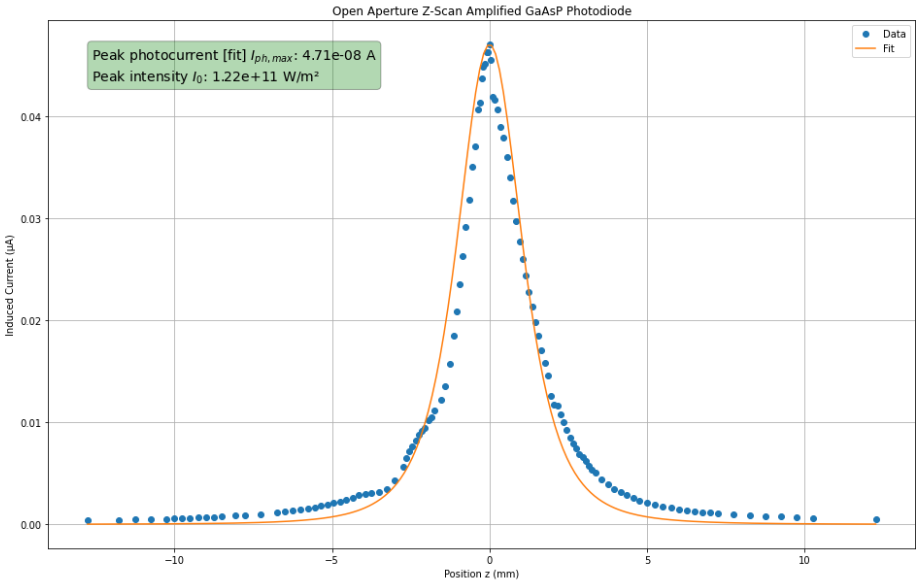

Figure 13: Z-Scan for amplified Yb NALM laser with an average power of 15 mW impinging onto the detector.

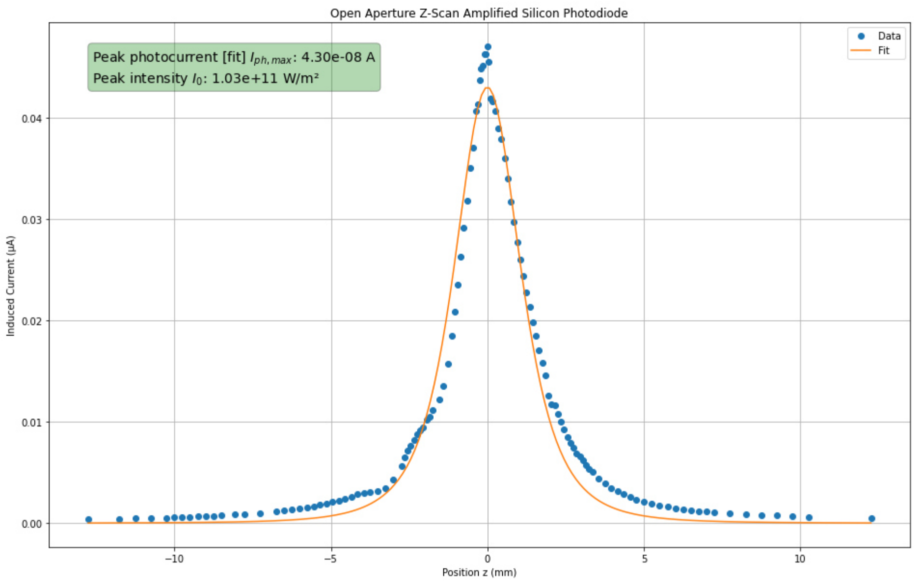

Figure 14: Z-Scan for the Er-DC system using a commercial Silicon Photodetector (Thorlabs PDA36A-EC at an average power impinging onto the detector of 2.5 mW. The 2PA coefficient was extracted to be $\alpha^{(2)} = 0.22$ cm/GW.

3.3 Interferometric Autocorrelation Results

The measurement in Figure (15) was taken with one arm of the Er-DC system, with an average power impinging onto the detector of (1.2 ± 0.06) mW using a commercial silicon photodetector (Thorlabs PDA36A-EC) with a gain setting of 70 dB, corresponding to a transimpedance gain of $4.75 \cdot 10^6$ V/A. The applied voltage to the speaker was 1 Hz at an applied frequency of 16 V. The theoretical peak-to-background ratio of 8:1 is almost reached perfectly, indicating proper alignment of the system.

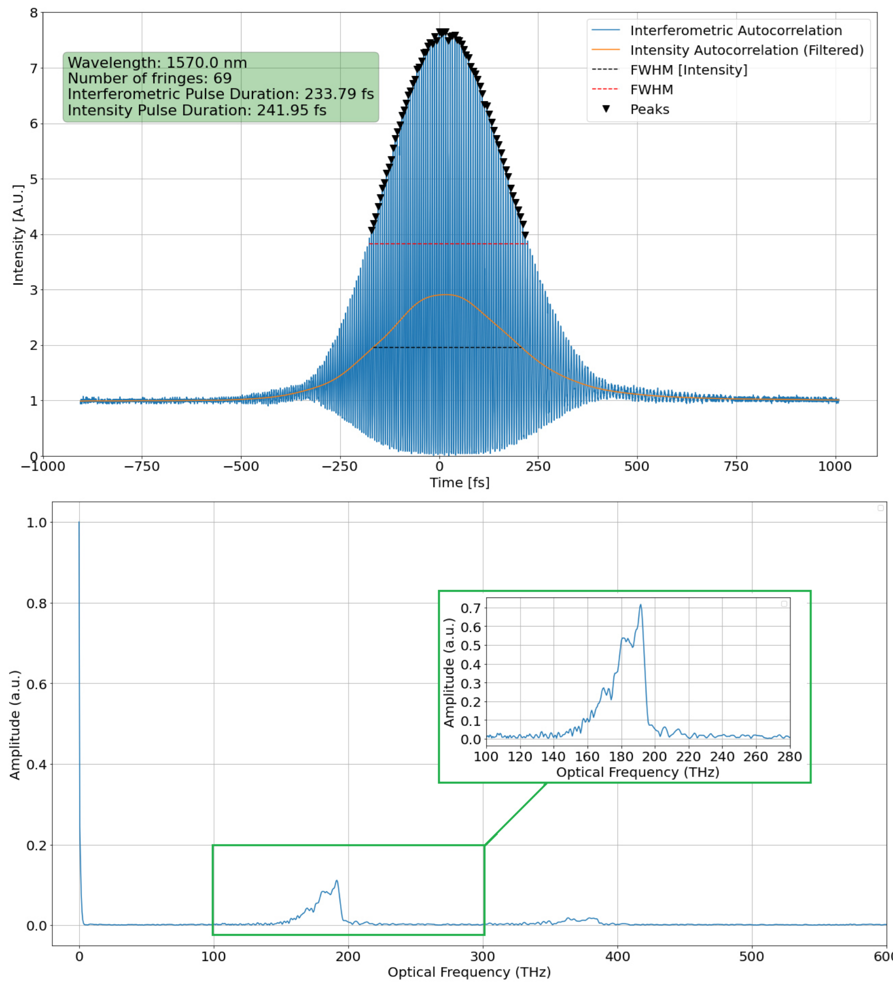

Figure 15: Top: Interferometric Autocorrelation measurement for one arm of the Erbium Dual Comb system. The peak-to-background ratio of 8:1 is clearly visible, indicating proper alignment. Bottom: Fourier transform of the 2PA Interferogram including zoom into the fundamental frequency. The intensity autocorrelation is retrieved by filtering out the fast oscillating terms, leaving only the DC component. The pulse duration was retrieved via fringe-counting and via the characterization of the delay stage, both of which produced FWHM pulse widths of 233 fs and 242 fs respectively, after application of the deconvolution factor.

The pulse duration was retrieved using the interferometric approach and the intensity approach. As for the interferometric approach, the number of fringes in the FWHM of Figure (15) was counted to be 69, with a center wavelength at $\lambda_{\text{center}} = 1.570$ µm. Each fringe corresponds to a time delay of 5.23 fs, giving an autocorrelation time of $\tau_{\text{AC}} = (360 \pm 10.46)$ fs. After application of the deconvolution factor for sech^2 pulses, this corresponds to a FWHM pulse duration of $\tau_{\text{P}} = 234$ fs. The uncertainty in the pulse duration retrieval stems from the imperfect 8:1 ratio, which underestimates the number of fringes in the FWHM and depends on alignment. Additionally, any chirp present in the pulse will automatically reduce the number of fringes, causing a tendency to underestimate the pulse duration using this approach.
Using the intensity approach, the pulse duration was retrieved to be $\tau_{\text{P}} = 242$ fs after application of the deconvolution factor. The spectral range was measured to be $\Delta\lambda = 20.1$ nm with a commercially available optical spectrum analyzer, yielding a time bandwidth product of 0.57 for the fringe-counting method and a value of 0.592 for the intensity approach, both are larger than the transform-limited case.

After mode-locking the system to a different state with a different spectral range, another pulse width measurement was taken, which yielded a pulse duration of (247 ± 10.46) fs using the interferometric approach and 239 fs using the intensity approach, shown in Figure (16), including a zoom into the fringes as well as the optical spectrum. The discrepancy between the two interferometric and the intensity value can again be attributed to an imperfect 8:1 ratio and alignment, as well as the slow onset of nonlinear motion of the delay stage as one approaches the turnaround points. Since each fringe corresponds to 5.23 fs, the difference between the two obtained values is within the measurement error of the method.

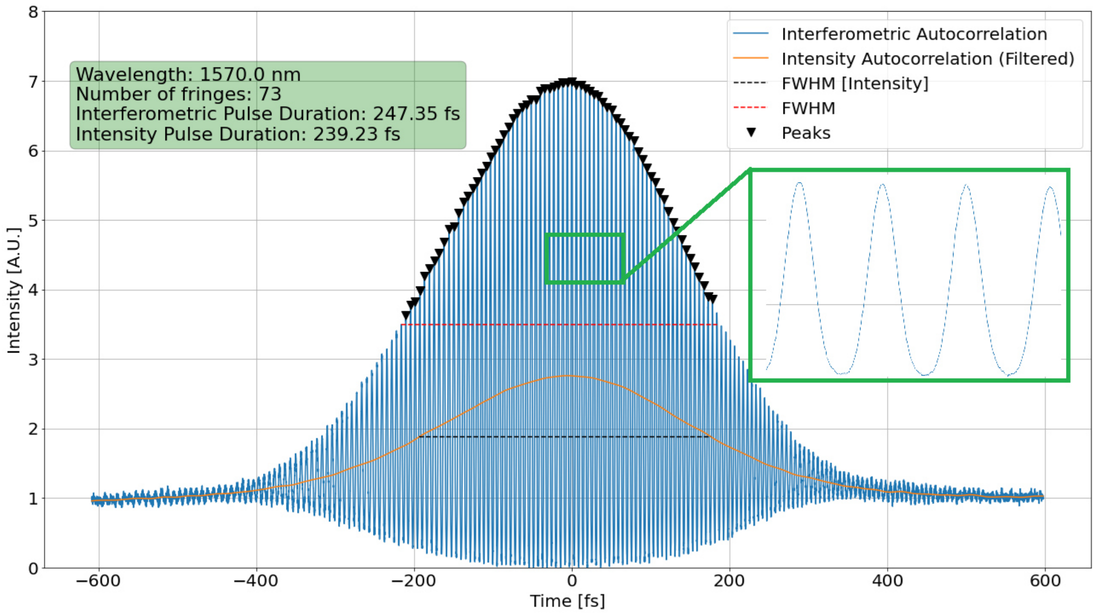

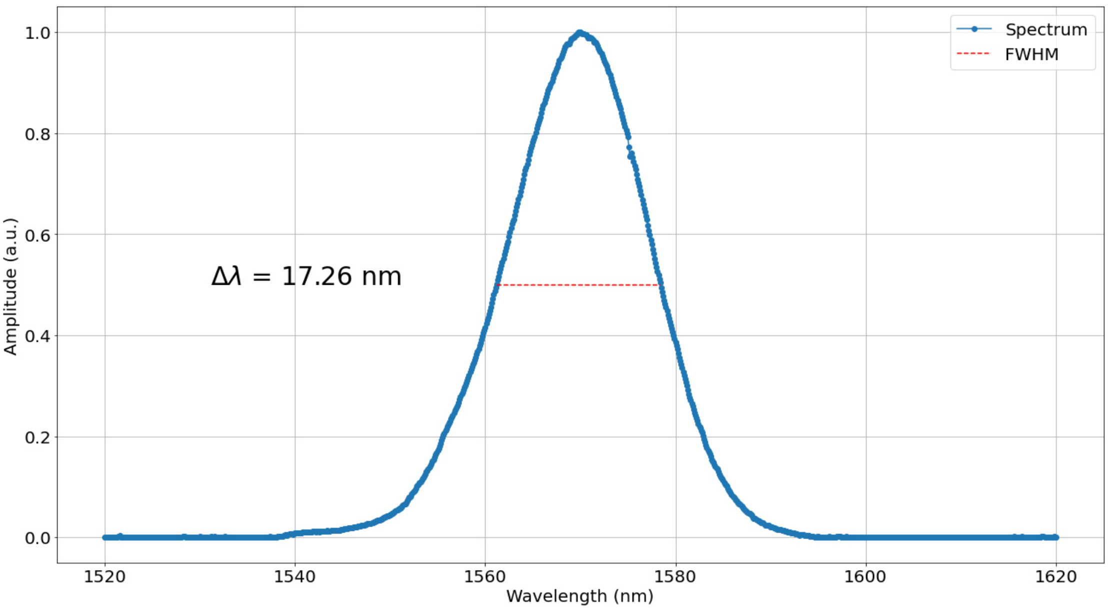

Figure 16: Autocorrelation measurements of the Er-DC laser system after it lost mode-locking and had to be re-started. Top: Interferometric autocorrelation trace (blue) and the respective FWHM (red dashed), including a zoom-in into the interference fringes, showing a pulse duration of ≈ 247 fs deploying the fringe counting method. The peaks of each individual fringe is marked with black triangles. The low-pass filtered intensity trace is plotted in orange, with its FWHM in dashed black, yielding a FWHM pulse duration of ≈ 239 fs. Bottom: Corresponding spectrum of the measurement, with the FWHM of 17.26 nm plotted. The time-bandwidth product for this state is 0.519 and 0.5 for the two approaches respectively.

Additionally, we aimed to measure the pulse duration at the maximum possible current settings for both diode drivers after 3 m of Er-40 and 1.8 m of Er-80 PM1550 fiber. However, the output of the laser system started to exhibit undesired multi-pulsing behavior as we increased the pump diodes, as can be seen in Figure 17.

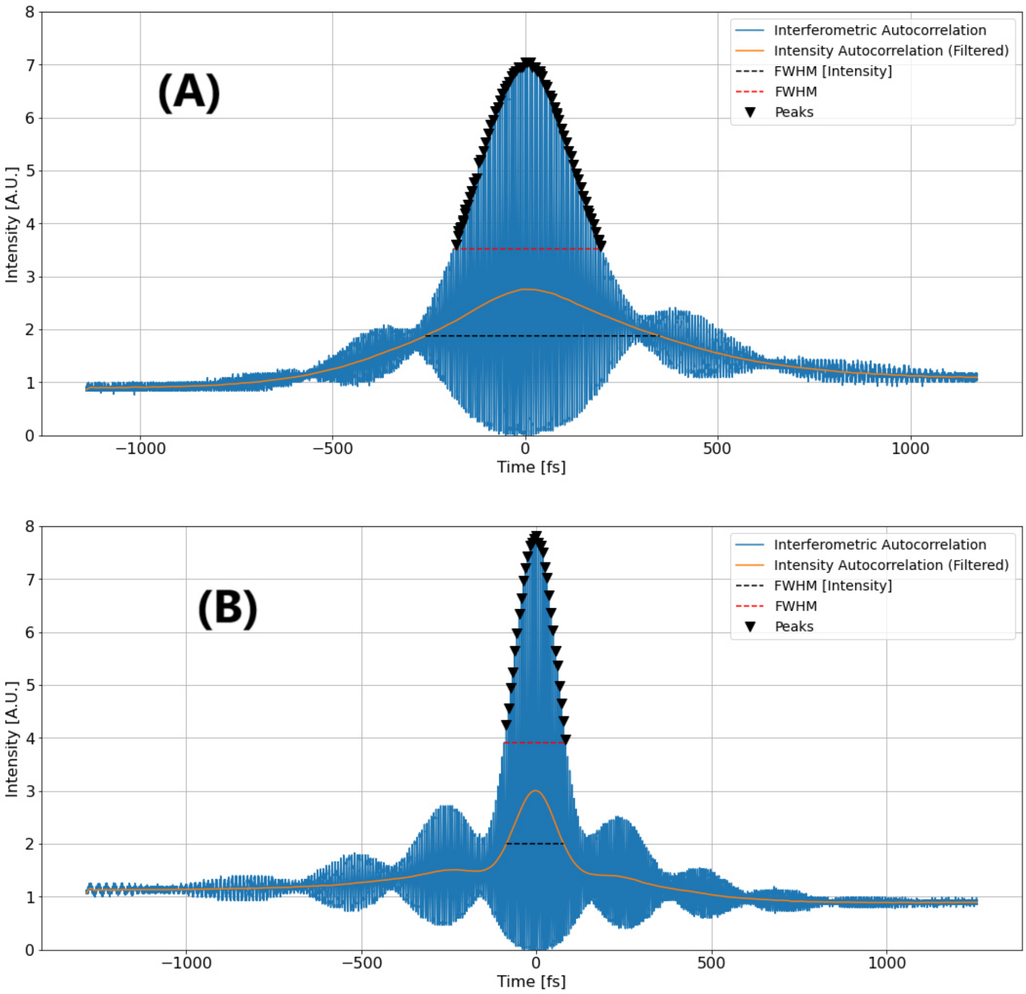

Figure 17: Observation of onset of multi-pulsing of the Er-DC system as diode currents are increased. (A): 700 mA pump currents on both diode drivers. The IAC trace starts to be smeared out into the intensity trace, indicating that the pulse is chirped (B): 700 mA on first diode driver, 1200 mA on the second amplification stage. The IAC trace starts to indicate multi-pulsing, which cannot be seen from the intensity trace alone.

The IAC trace was also measured for the amplified Yb-NALM system. The power impinging onto the detector after amplification was (15 ± 2.5) mW. The central wavelength of the spectrum was measured to be $\lambda_{\text{center}} = 1042$ nm with a spectral width of $\Delta\lambda = 13$ nm before amplification. The interferogram and its Fourier transform are given in Figure (18):

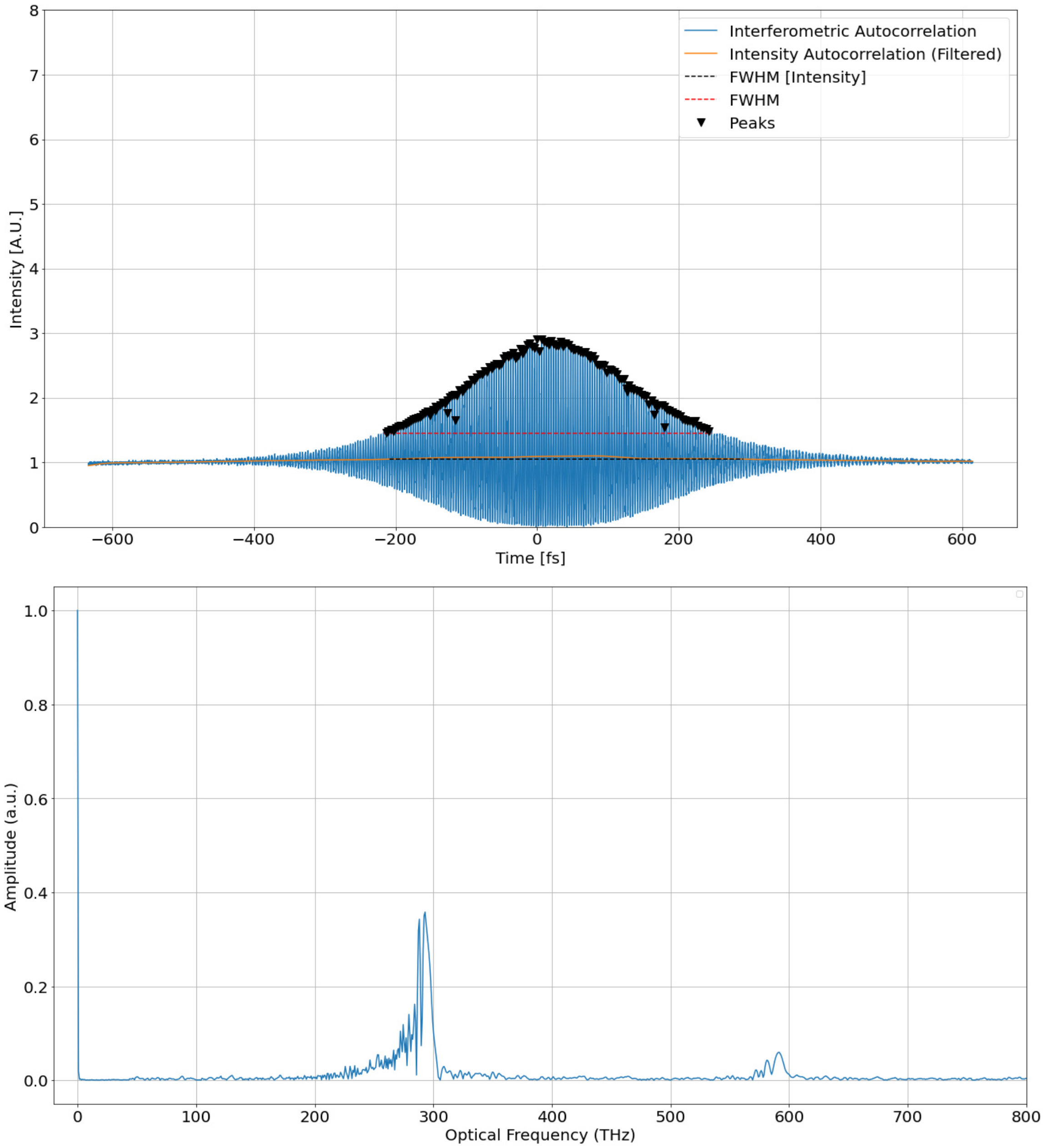

Figure 18: Top: 2PA Interferometric Autocorrelation Trace for the amplified Yb-NALM system using the GaAsP detector including transimpedance amplifier. Bottom: Fourier transform of the 2PA interferogram.

Even though the peak-to-background ratio was larger than 2:1, indicating a nonlinear response of the detector, the peak-to-background ratio was capped at a value of about 3:1, even after several attempts of re-alignment. Several measurements were performed for different settings of the delay stage in order to average out any errors due to noise. Averaging out ten interferograms, the number of fringes in the FWHM was counted to be 141, giving an autocorrelation time of $\tau_{\text{AC}} = 489$ fs, yielding a pulse duration of about 317 fs after application of the deconvolution factor, assuming a sech^2 pulse shape. The intensity approach produced a similar result; however, it should be noted that due the small nonlinearity, the actual value of the FWHM will be overestimated severely. The TBP product of this measurement yields a value of 1.19, almost four times the transform-limited case.

4 Conclusion and Discussion

In this thesis, an easy-to-implement pulse duration retrieval method based on interferometric autocorrelation using 2-photon absorption in semiconductors was successfully assembled and tested. Measurements were performed for 2 different laser systems operating at wavelengths in the near-IR at 1.04 µm and at 1.57 µm. The theoretical concept extends into even longer wavelength regimes, showing the large possible application range of this method. The measured pulse duration for the Er-DC system was 233 fs and 247 fs using two different approaches at a spectral width $\Delta\lambda = 20.1$ nm. A new set of measurements was performed as the laser had lost its mode-locked state and yielded FWHM pulse durations of 247 fs and 239 fs respectively at a spectral width of $\Delta\lambda = 17.26$ nm. Both measurements reached the theoretical 8:1 peak-to-background ratio almost perfectly, indicating that the interferometer was aligned properly. The FWHM values were extracted using the intensity and the interferometric approach, with the discrepancy between the two values being within the measurement error of ≈ 10 fs. We additionally observed undesired multi-pulsing in the Er-DC system at higher pump currents, limiting the characterization of pulse widths under these conditions. Since the IAC is symmetric, $\Gamma_{\text{IAC}}(\tau) = \Gamma_{\text{IAC}}(-\tau)$, there is no way to detect whether the multi-pulses arise due to pre- or due to post-pulsing. An approach to determine whether it is in fact pre- or post-pulsing would be to perform an additional IAC measurement using a 3PA detector and comparing this obtained trace to the trace obtained from 2PA. However, the induced 3PA current would be even smaller than the 2PA current, meaning that this is impractical for low-power laser systems.

Unfortunately the bandwidth of the GaAsP photodetector was not enough to properly resolve the interference fringes of the seed laser; nevertheless, the pulse width was measured after optical amplification using the intensity approach, which yielded a pulse duration of ≈ 317 fs. However, the nonlinear signal induced in the photodiode was insufficient and the imperfect peak-to-background ratio was only 3:1, such that any statement about pulse duration should be taken with special care. Additionally, the dependence of the induced 2PA photocurrent on average power was investigated and showed the expected slope of 1.907 across almost two orders of magnitudes for the silicon photodetector. As for the GaAsP diode, the obtained slope was 1.891 for powers from 1 mW to 15 mW, indicating that for both diodes the majority of induced current can be attributed to 2PA only. The actually induced photocurrent for the GaAsP photodetector was measured to be much smaller than the theoretical prediction.

The 2PA coefficient $\alpha^{(2)}$ was extracted for the silicon detector, whose experimental value of $\alpha^{(2)} = 2.2 \cdot 10^{-11}$ m/W is in agreement with other experimental values, but off from the theoretical value of $2 \cdot 10^{-10}$ m/W by one order of magnitude. Unfortunately the discrepancy was even larger for the case of GaAsP diode, whose experimental 2PA coefficient was extracted to be $3.2 \cdot 10^{-13}$ m/W, off by almost 2 orders of magnitude from the expected theoretical value of $6 \cdot 10^{-11}$ m/W. This discrepancy might also be the reason for the much smaller induced 2PA current than theoretically predicted.

Error minimization could be performed with a more sophisticated delay stage (e.g. a piezo), as it would allow for more precise control over the step sizes. Increasing the linear displacement of the delay stage would also allow for characterization of longer pulses, as the autocorrelator is currently limited to about FWHM pulse durations of about 1 ps. Although this seems promising, longer pulse durations will also induce smaller 2PA currents to the point where it will be indistinguishable from noise, highlighting the importance of using an appropriate detector and amplification mechanism.

Finally, when coming to post-processing of the data, special care should also be taken when deploying the fringe counting method using an algorithm as the software that is used to extract the peaks might be prone to over-counting peaks when the SNR is not sufficient.

Summarizing, the viability of using 2PA as a base for nonlinear frequency conversion for autocorrelation measurements was theoretically outlined and experimentally demonstrated. Due to the fact that phase-matching between the two propagating beams is not required in 2PA, this approach offers a more efficient way to measure pulse durations over a wider range of wavelengths using a single detector in a relatively simple setup.

A Appendix - Noise Analysis Amplifier Circuit

Three main noise sources contribute to the total noise of the transimpedance amplifier photodetector system, namely the photodiode, the operational amplifier as well as the feedback resistor.

All of the current noise sources can be treated as separate systems [24], such that

$$i_{\text{Total}} = \sqrt{i_{\text{Photodiode}}{}^2 + i_{\text{TIA}}{}^2} \tag{54}$$

The total output RMS noise voltage $E_{\text{Noise, RMS}}$ depends on the value of the feedback resistor R_{F} and the noise bandwidth Δf via

$$E_{\text{Noise, RMS}} = e_{\text{Total}}\sqrt{\Delta f} = i_{\text{Total}} R_{\text{F}} \sqrt{\Delta f} \tag{55}$$

where the noise bandwidth Δf depends on the cutoff-frequency f_{C} via $\Delta f = f_{\text{C}} \cdot \pi/2 = \frac{1}{4R_{\text{F}}C_{\text{F}}}$.

The contributions to the noise curve from the photodiode include the thermal noise due to the shunt resistance R_{Sh} as well as the shot noise arising from the photodiodes dark current:

$$i_{\text{n, PD}} = \sqrt{i_{\text{s, Dark}}{}^2 + i_{\text{Sh}}{}^2} = \sqrt{2qI_{\text{Dark}} + 4k_{\text{B}}T/R_{\text{Sh}}} \tag{56}$$

Random movement of charge carriers inside the (feedback) resistor contribute to thermal noise (also known as Johnson noise) via

$$i_{\text{n, Johnson}} = \sqrt{\frac{4k_{\text{B}}T}{R_{\text{F}}}} \tag{57}$$

Finally, the contribution of the operational amplifier depends on its broadband current noise density as well as its broadband noise voltage density, both of which can typically be found in the manufacturers datasheet. For the first transimpedance amplifier, an OPA828 by Texas instruments was used, whose specs can be found in Table (3)

The noise gain will be mostly determined by the feedback capacitor C_{F} and the input capacitances $C_{\text{in}} = C_{\text{OPA}} + C_{\text{Diode}}$, as they will cause a peak in the noise gain curve which will significantly affect the total output noise voltage. In order to carry out the full noise analysis, further frequency parameters have to be investigated. The noise gain curve will have a zero-frequency pole at

$$f_{\text{Z}} = \frac{1}{2\pi R_{\text{F}}(C_{\text{F}} + C_{\text{in}})} \tag{58}$$

for frequencies > f_{Z}, the noise gain will be 20 dB/decade if no feedback capacitor is included in the system. By adding a feedback capacitor to the system, the noise gain curve will flatten out after f_{Total}, i.e. at the intersection between the noise gain and the open loop gain, f_{i}:

$$f_{\text{i}} = \frac{C_{\text{F}}}{_{\text{F}} + C_{\text{in}}} \cdot f_{\text{t}} \tag{59}$$

where f_{t} is the unity gain frequency (gain bandwidth product) of the OPA, also given in Table (2).

Finally, the intersection frequency between the $1/f$ noise and the broadband noise is given by

$$f_{\text{f}} = (\frac{e_{\text{fnorm}}}{e_{\text{BB}}})^2 \tag{60}$$

with e_{fnorm} as OPA noise contribution at 0.1 Hz. All of these frequency parameters contribute to the total output RMS noise voltage of the OPA individually. The different frequency components will experience a different noise gain, depending on the frequency regime of the signal.

Table (2) provides all key parameters required for the noise analysis of the photodetector system:

Parameter	Value
Photodiode	Hamamatsu G1115
Dark Current	4 pA
Junction Capacitance	300 pF
Shunt Resistance	80 MΩ
Feedback Resistance	1 MΩ
Feedback Capacitance	3.53 nF
TIA OPA	Texas Instruments OPA828
GBP	45 MHz
Differential Mode Input Capacitance	6 pF
Common Mode Input Capacitance	9 pF
Current Noise Density	1.2 fA/$\sqrt{Hz}$
Current Voltage Density	4.8 nV/$\sqrt{Hz}$
Non-Inverting Amplifier	AD797
GBP	110 MHz
Differential Mode Input Capacitance	20 pF
Common Mode Input Capacitance	5 pF
Current Noise Density	2.0 pA/$\sqrt{Hz}$
Current Voltage Density	0.9 nV/$\sqrt{Hz}$

Table 2: Components used to construct the photodetector as well as their key parameters characterizing the noise performance of the system.

The total contribution to the current noise spectral density due to the photodiode is given by equation (56),

$$i_{\text{n, PD}} = \sqrt{(1.13fA/\sqrt{Hz})^2 + (14.1fA/\sqrt{Hz})^2} = 14.14fA/\sqrt{Hz} \tag{61}$$

including the contribution of the OPA via equation 54, the current noise spectral density of the electronic system is given by

$$i_{\text{n, Total}} = \sqrt{(14.14fA/\sqrt{Hz})^2 + (1.2fA/\sqrt{Hz})^2} = 14.19fA/\sqrt{Hz} \tag{62}$$

This current will flow through the feedback resistor, yielding a output noise voltage spectral density of

$$e_{\text{i,n, Total}} = i_{\text{n, Total}} \cdot R_{\text{F}} = 14.19\ nV/\sqrt{Hz} \tag{63}$$

Finally, the total RMS output voltage noise due to OPA and photodiode:

$$E_{\text{i, n, Total}} = e_{\text{i, n, Total}} \cdot \sqrt{\Delta f} = 14.19nV/\sqrt{Hz} \cdot \sqrt{70Hz} = 118.72\ nV_{\text{RMS}} \tag{64}$$

The total RMS output voltage noise due to the feedback resistor depends on equation 57 and is $E_{\text{R, n, Total}} = i_{\text{n, Johnson}} R_{\text{F}} \sqrt{\Delta f} = 1.07\ \mu V_{\text{RMS}}$

Parameter	Value
f_{C}	45 Hz
Δf	70 Hz
f_{Z}	53 Hz
f_{t}	45 MHz
f_{i}	41.3 MHz
f_{f}	15.66 Hz
f_{L}	0.1 Hz

Table 3: Important frequency poles of the photodetector system.

The contributions due to OPA noise voltage, which depends on the frequency parameters given in Table (3).

The RMS noise contributions for the individual frequency regimes is given by

$$E_{\mathrm{N,\ V1}} = e_{\mathrm{BB}} \cdot \sqrt{f_{\mathrm{f}} \cdot \ln \frac{f_{\mathrm{f}}}{f_{\mathrm{L}}}} = \frac{4.8nV}{\sqrt{Hz}} \cdot \sqrt{15.66Hz \cdot \ln \frac{15.66}{0.1}} = 42.6\ nV_{\mathrm{RMS}} \tag{65}$$

$$E_{\mathrm{N,\ V2}} = e_{\mathrm{BB}} \cdot \sqrt{f_{\mathrm{Z}} - f_{\mathrm{f}}} = \frac{4.8nV}{\sqrt{Hz}} \cdot \sqrt{53Hz - 15.66Hz} = 29\ nV_{\mathrm{RMS}} \tag{66}$$

$$E_{\mathrm{N,\ V3}} = e_{\mathrm{BB}} \cdot \sqrt{\frac{{f_{\mathrm{c}}}^3 - {f_{\mathrm{Z}}}^3}{3{f_{\mathrm{Z}}}^2}} = \frac{4.8nV}{\sqrt{Hz}} \cdot \sqrt{\frac{{f_{\mathrm{C}}}^3 - {f_{\mathrm{Z}}}^3}{3{f_{\mathrm{Z}}}^2}} = 498\ nV_{\mathrm{RMS}} \tag{67}$$

$$E_{\mathrm{N,\ V4}} = e_{\mathrm{BB}} \cdot (1 + \frac{C_{\mathrm{in}}}{C_{\mathrm{F}}}) \cdot \sqrt{f_{\mathrm{i}} - f_{\mathrm{c}}} = \frac{4.8nV}{\sqrt{Hz}} \cdot \sqrt{1 + \frac{C_{\mathrm{in}}}{C_{\mathrm{F}}}) \cdot \sqrt{f_{\mathrm{i}} - f_{\mathrm{c}}}} = 4.8\ nV_{\mathrm{RMS}} \tag{68}$$

$$E_{\mathrm{N,\ V5}} = e_{\mathrm{BB}} \cdot \sqrt{\frac{{f_{\mathrm{t}}}^2}{f_{\mathrm{i}}}} = \frac{4.8nV}{\sqrt{Hz}} \cdot \sqrt{\frac{45MHz^2}{41.3MHz}} = 33.6\mu V_{\mathrm{RMS}} \tag{69}$$

Giving a total of individual noise contributions

$$E_{\mathrm{N,\ V,\ Total}} = \sqrt{\sum_i E_{\mathrm{N,\ V}_i}} = 3.29\ mV_{\mathrm{RMS}} \tag{70}$$

and finally, the total output noise voltage

$$E_{\mathrm{n,\ Total}} = \sqrt{{E_{\mathrm{N,\ V,\ Total}}}^2 + {E_{\mathrm{R,\ N,\ Total}}}^2 + {E_{\mathrm{i,\ n,\ Total}}}^2} = 3.3mV_{\mathrm{RMS}} \tag{71}$$

from this one can see that the biggest contribution to noise stems from the OPA and contributions from other components can be mostly neglected.

When using the second-stage as well, the noise of the second operational amplifier has to be considered as well. For the non-inverting amplifier configuration, any noise gain is equal to the signal gain, i.e. it will also follow the $1 + \frac{R_2}{R_1}$ rule. In particular, the noise contribution due to R_1 is given by

$$E_{\mathrm{n,\ R_1}} = 4k_{\mathrm{B}}TR_1\frac{{R_1}^2}{{R_1}^2 + {R_2}^2} \tag{72}$$

Resistor R_2 gives the same contribution with indices 1 and 2 swapped. The total noise contribution due to these two feedback resistors is given by

$$E_{\mathrm{n}} = 4k_{\mathrm{B}}T\frac{R_1R_2}{R_1 + R_2} \tag{73}$$

When using high gain configurations (gain larger than 2) the noise gain contribution due to R_2 will always be larger than that from R_1, even though typically $R_2 < R_1$.

Just like the single-stage transimpedance amplifier, voltage noise and current noise arise due to the cascaded operational amplifier, which will contribute to the total spectral noise density, which can be added to the total system noise by taking the square of all contributions, summing them up and taking the square root.
Given that the measured voltage signal is given by E_{Signal}, the SNR can be calculated via

$$SNR = 20\log{(\frac{E_{\mathrm{Signal}}}{E_{\mathrm{n,Total}}})} \tag{74}$$

meaning that for the noise contribution of 3.3 $\mathrm{mV_{Total}}$ and a transimpedance gain of 10^6 V/A, the induced current should be at least 33 nA in order to obtain a SNR of $<$ 20 dB.

B Appendix 2 - Table of abbreviations

Abbreviation	Definition
2PA	2-Photon Absorption
3PA	3-Photon Absorption
CW	Continuous Wave
DC	Direct Current
Er-DC	Erbium Dual-Comb
FRAC	Fringe-Resolved Autocorrelation
FROG	Frequency-Resolved Optical Gating
FTS	Fourier Transform Spectroscopy
FWHM	Full-Width Half-Maximum
GDD	Group Delay Dispersion
GVD	Group Velocity Dispersion
IAC	Interferometric Autocorrelation
NALM	Nonlinear Amplifying Loop Mirror
OPD	Optical Path Difference
PMT	Photo-Multiplier Tube
SHG	Second-Harmonic Generation
SNR	Signal-to-Noise Ratio
SPIDER	Spectral Phase Interferometry for Direct Electric-Field Reconstruction
TBP	Time-Bandwidth Product
TIA	Transimpedance Amplifier
THG	Third-Harmonic Generation
OPA	Operational Amplifier

C References

[1] Jun Ye and Steven T Cundiff. *Femtosecond optical frequency comb: principle, operation and applications*. Springer Science & Business Media, 2005.

[2] Maria Göppert. Über die Wahrscheinlichkeit des Zusammenwirkens zweier Lichtquanten in einem Elementarakt. *Naturwissenschaften*, 17(48):932–932, 1929.

[3] W. Kaiser and C. G. B. Garrett. Two-Photon Excitation in CaF_2: Eu^{2+}. *Phys. Rev. Lett.*, 7:229–231, Sep 1961.

[4] LP Barry, PG Bollond, JM Dudley, JD Harvey, and Rainer Leonhardt. Autocorrelation of ultrashort pulses at 1.5 μm based on nonlinear response of silicon photodiodes. *Electronics Letters*, 32(20):1922–1923, 1996.

[5] Kazuro Kikuchi. Highly sensitive interferometric autocorrelator in the optical communication band using si avalanche photodiode as two-photon absorber. In *Optical Fiber Communication Conference*, page ThN4. Optica Publishing Group, 1998.

[6] Hyung-Sik Kim and Yong-Sik Lim. Optical Autocorrelation Measurement for Ultrafast Pulses at NIR Wavelengths Using GaP, GaAsP, and Si Photoconductive Detectors. *Applied Sciences*, 13(12):6957, 2023.

[7] Chris Xu, Jeffrey Roth, and Wayne Knox. Ultra-sensitive autocorrelation of 1.5 m light with single photon counting silicon avalanche photodiode. *Electronics Letters*, 38:86 – 88, 02 2002.

[8] Patrick Langlois and Erich P Ippen. Measurement of pulse asymmetry by three-photon-absorption autocorrelation in a GaAsP photodiode. *Optics letters*, 24(24):1868–1870, 1999.

[9] Jianming Dai, H Teng, and Chunlei Guo. Second-and third-order interferometric autocorrelations based on harmonic generations from metal surfaces. *Optics communications*, 252(1-3):173–178, 2005.

[10] Aline S. Mayer, Wilfrid Grosinger, Jakob Fellinger, Georg Winkler, Lukas W. Perner, Stefan Droste, Sarper H. Salman, Chen Li, Christoph M. Heyl, Ingmar Hartl, and Oliver H. Heckl. Flexible all-PM NALM Yb:fiber laser design for frequency comb applications: operation regimes and their noise properties. *Opt. Express*, 28(13):18946–18968, Jun 2020.

[11] P. E. Collin Aldia, Lukas W. Perner, Jonas K. C. Ballentin, Zbigniew Łaszczych, Monika Bahl, and Oliver H. Heckl. Demonstration of Viability for Dual Comb Spectroscopy Using an Erbium Dual Comb Fiber Laser Based on Polarization Multiplexing. In *CLEO 2024*, page SF1Q.6. Optica Publishing Group, 2024.

[12] C. Iaconis and I. A. Walmsley. Spectral phase interferometry for direct electric-field reconstruction of ultrashort optical pulses. *Opt. Lett.*, 23(10):792–794, May 1998.

[13] D.J. Kane and R. Trebino. Characterization of arbitrary femtosecond pulses using frequency-resolved optical gating. *IEEE Journal of Quantum Electronics*, 29(2):571–579, 1993.

[14] Ursula Keller and R Paschotta. *Ultrafast lasers*. Springer, 2021.

[15] EZ Chong, TF Watson, and F Festy. Autocorrelation measurement of femtosecond laser pulses based on two-photon absorption in GaP photodiode. *Applied Physics Letters*, 105(6), 2014.

[16] Seong-Il Shin and Yong-Sik Lim. Simple autocorrelation measurement by using a GaP photoconductive detector. *Journal of the Optical Society of Korea*, 20(3):435–440, 2016.

[17] Torben Fiehler, Clara Saraceno, Günter Steinmeyer, and Ulrich Wittrock. Pitfall in autocorrelation measurements of laser radiation. *Opt. Express*, 32(21):36811–36823, Oct 2024.

[18] Shanti Toenger, Roosa Mäkitalo, Jani Ahvenjärvi, Piotr Ryczkowski, Mikko Närhi, John M Dudley, and Goëry Genty. Interferometric autocorrelation measurements of supercontinuum based on two-photon absorption. *JOSA B*, 36(5):1320–1326, 2019.

[19] Jean-Claude M Diels, Joel J Fontaine, Ian C McMichael, and Francesco Simoni. Control and measurement of ultrashort pulse shapes (in amplitude and phase) with femtosecond accuracy. *Applied Optics*, 24(9):1270–1282, 1985.

[20] F Hache, TJ Driscoll, M Cavallari, and GM Gale. Measurement of ultrashort pulse durations by interferometric autocorrelation: Influence of various parameters. *Applied optics*, 35(18):3230–3236, 1996.

[21] Govind Agrawal. Chapter 3 - group-velocity dispersion. In Govind Agrawal, editor, *Nonlinear Fiber Optics (Fifth Edition)*, Optics and Photonics, pages 57–85. Academic Press, Boston, fifth edition edition, 2013.

[22] Bahaa EA Saleh and Malvin Carl Teich. *Fundamentals of Photonics*. John Wiley & Sons, 2019.

[23] R.W. Boyd. *Nonlinear Optics*. Elsevier Science, 2020.

[24] Philip CD Hobbs. *Building Electro-Optical Systems: making it all work*. John Wiley & Sons, 2022.

[25] Toshiaki Kagawa. Two-photon absorption in photodiodes. *Photodiode: From Fundamentals to applications*, 10:50491, 2012.

[26] Hernando Garcia and Ramki Kalyanaraman. Phonon-assisted two-photon absorption in the presence of a DC-field: the nonlinear Franz–Keldysh effect in indirect gap semiconductors. *Journal of Physics B: Atomic, Molecular and Optical Physics*, 39(12):2737, 2006.

[27] BS Wherrett. Scaling rules for multiphoton interband absorption in semiconductors. *JOSA B*, 1(1):67–72, 1984.

[28] Eric W Van Stryland, MA Woodall, H Vanherzeele, and MJ Soileau. Energy band-gap dependence of two-photon absorption. *Optics letters*, 10(10):490–492, 1985.

[29] Marco Piccardo, Noah A Rubin, Lauren Meadowcroft, Paul Chevalier, Henry Yuan, Joseph Kimchi, and Federico Capasso. Mid-infrared two-photon absorption in an extended-wavelength InGaAs photodetector. *Applied Physics Letters*, 112(4), 2018.

[30] CR Pidgeon, BS Wherrett, AM Johnston, J Dempsey, and Alan Miller. Two-photon absorption in zinc-blende semiconductors. *Physical Review Letters*, 42(26):1785, 1979.

[31] Alan D Bristow, Nir Rotenberg, and Henry M Van Driel. Two-photon absorption and Kerr coefficients of silicon for 850–2200nm. *Applied physics letters*, 90(19), 2007.

[32] H. K. Tsang, C. S. Wong, T. K. Liang, I. E. Day, S. W. Roberts, A. Harpin, J. Drake, and M. Asghari. Optical dispersion, two-photon absorption and self-phase modulation in silicon waveguides at 1.5m wavelength. *Applied Physics Letters*, 80(3):416–418, 01 2002.

[33] T. Boggess, K. Bohnert, K. Mansour, S. Moss, I. Boyd, and A. Smirl. Simultaneous measurement of the two-photon coefficient and free-carrier cross section above the bandgap of crystalline silicon. *IEEE Journal of Quantum Electronics*, 22(2):360–368, 1986.

[34] M. Sheik-Bahae, D.C. Hutchings, D.J. Hagan, and E.W. Van Stryland. Dispersion of bound electron nonlinear refraction in solids. *IEEE Journal of Quantum Electronics*, 27(6):1296–1309, 1991.

[35] John J McFerran, John Winterflood, Clinton Burton, and Andre N Luiten. Resonant interferometric autocorrelator for estimation of laser pulse duration. *Review of scientific instruments*, 76(1), 2005.

[36] Tecla Gabbrielli, Giacomo Insero, Michele De Regis, Nicola Corrias, Iacopo Galli, Davide Mazzotti, Paolo Bartolini, Jeong Hyun Huh, Carsten Cleff, Alexander Kastner, et al. Time/frequency-domain characterization of a mid-IR DFG frequency comb via two-photon and heterodyne detection. *Optics Express*, 31(21):35330–35342, 2023.

[37] Christian Spielmann, Lin Xu, and Ferenc Krausz. Measurement of interferometric autocorrelations: comment. *Applied optics*, 36(12):2523–2525, 1997.

[38] AK Sharma, PA Naik, and PD Gupta. Real-time autocorrelator with enhanced temporal scan range for measurements of ultrashort laser pulses. *Optics & Laser Technology*, 39(3):465–469, 2007.